UNIVERSITÀ DEGLI STUDI FIRENZE

Scuola di Scienze Matematiche, Fisiche e Naturali

Corso di laurea in Scienze Fisiche e Astrofisiche

Coherent Dynamics of ^{6}Li Superfluid Fermi Gases within a Double-Well Potential across the BEC-BCS Crossover

Dinamica coerente di gas fermionici superfluidi di ^{6}Li in un potenziale a doppia buca attraverso il crossover BEC-BCS

Relatore: Dott. Matteo Zaccanti

Correlatore: Prof. Massimo Inguscio

Candidato: Elettra Neri

Anno accademico 2013-2014

Contents

Chapter 1

Introduction

How a superfluid flow is affected, and eventually impeded, by the presence of a constriction, and more generally by an obstacle, represents a fundamental question dating back to the early days of investigation of superfluidity and superconductivity. Very importantly, this issue lays at the heart of the seminal works of Landau [1], Feynman [2, 3] and Anderson [4]. Paradigmatic examples of phenomena originating from such a scenario are represented by the Josephson effect [5], with the onset of pair breaking effects and of quantized vortices [6, 7] in superconducting junctions, by phase slippage and vortex nucleation in superfluid Helium 4 [8], and more recently by Josephson oscillations and macroscopic quantum self-trapping in atomic and polariton BECs [9, 10, 11, 12, 13, 14]. In this framework, understanding the interplay between coherent superfluid and dissipative dynamics is still nowadays subject of an intense, multidisciplinary research activity, also connected with the development of novel superfluid/superconductor-based sensor devices [15].

In the field of ultracold gases, the dynamics of BEC-BCS crossover Fermi superfluids [16, 17, 18] in the presence of thin optical barrier potentials, have attracted a lot of attention over the last decade [19, 20, 21, 22]. In fact, such systems are extremely appealing since they represent a clean and controllable environment in which all the major phenomena mentioned above can in principle be studied in a continuous manner, and with the high degree of accuracy peculiar of a quantum gas experiment.

On the BEC side of the crossover, where the superfluid Fermi gas is condensed in tightly bound bosonic molecules, the system can be regarded as a strongly interacting Bose liquid. In contrast with usual atomic Bose Einstein condensates, such molecular superfluid turns out being extraordinarily stable against inelastic decay in the region of strong inter-particle interaction, and it can in principle be employed for the study and the simulation of quantum phenomena occurring in the dense superfluid phase of liquid ^{4}He.

On the BCS side of the crossover, where superfluidity arises from the Cooper pairing instability, the macroscopic behavior of an ultracold Fermi superfluid mimics the one of a conventional superconductor. In particular, in this limit one can experimentally investigate a variety of effects related to the fermionic, composite nature of the superfluid pairs, and their influence on the system dynamics.

Finally, in the intriguing region around the crossover, where the interparticle interaction is maximally strong, reaching the ultimate limit allowed by quantum dynamics, the unitary Fermi gas represents a unique environment for investigating many-body phenomena peculiar of strongly correlated superfluid systems, such as high-Tc superconducting materials.

In this thesis, I report on the first experimental thorough investigation of the dynamics of a trapped superfluid Fermi gas composed of Lithium6 atom pairs, in the presence of a thin barrier potential. Inter-particle interactions are magnetically tuned via the Feshbach resonance phenomenon [23, 24]. The height of the barrier is set and controlled by adjusting the power of a laser beam imprinted on the ultracold cloud confined in a harmonic trap, and that is blue-detuned for both Lithium atoms and pairs, hence acting as a repulsive potential. Such a potential is shaped in such a way to create a strongly asymmetric sheet of light, characterized by a long waist greatly exceeding the ultracold cloud dimensions, and by a micron-sized short waist, which is only few times larger than the mean inter-particle spacing of the superfluid system.

The main results obtained in this work are the following:

- In the limit of high barriers and small amplitude flows we could measure the plasma frequency ω_p characterizing superfluid Josephson oscillations throughout the BEC-BCS crossover.

- From the experimental determination of ω_p, combined with the knowledge of the equation of state of our system [25, 26], we derive the qualitative behavior of the maximum Josephson current supported by the superfluid Fermi gas, finding that it is maximum for unitary limited interactions, in agreement with recent theoretical investigations [27, 19].

- Exiting the small amplitude limit, we access a different dynamical regime characterized by a "running phase" of the superfluid order parameter [8, 13], within which the superfluid current is quenched. We find that the entrance into such a regime is accompanied for our system by propagation of (solitonic) vortices [28, 29, 26] throughout the superfluid bulk, induced by phase-slip dynamics [8].

The thesis is organized as it follows: In Chapter 2 I briefly recall some basic concepts of scattering theory and their specific application to the regime of ultracold collisions. I introduce the reader to the phenomenon of the Feshbach resonance, and I also provide an intuitive and qualitative picture of the BEC-BCS crossover scenario.

Chapter 3 describes the different dynamical regimes expected for a superfluid flow evolving within a double well potential, with special emphasis to the aspects that are specific of our system. In particular, the description of the superfluid dynamics based on the so-called two-mode approximation [9] provides a simple and easy-to-handle theoretical frame for understanding the various regimes occurring on the BEC limit of the crossover. How and under which circumstances such an approximation is no longer valid and ceases to hold is then discussed.

In Chapter 4 I report on the details of our experimental setup: in particular, I describe the parts of the apparatus built up and characterized during the period of my thesis, namely the optical barrier potential, together with the experimental protocols employed for the study of the superfluid dynamics. In particular, I describe a simple model that I developed for describing the transmission of a quantum particle through a barrier potential. This basic theory approach allowed us to find out an efficient method to focus the sheet of light on the ultracold trapped sample.

Finally, in Chapter 5 I present the experimental results obtained so far in the lab. A detailed discussion concerning the acquisition and the analysis of the data is provided, together with their interpretation based on currently available theory approaches.

Chapter 2

Ultracold Fermionic Superfluids

A major challenge of contemporary physics is the study of the wealth of phases occurring in larges ensamble modes of interacting quantum particles. To this purpose ultracold dilute atomic gases represent a powerful experimental tool, thanks to the high degree of control over all the relevant parameters that set both the static and dynamic behaviour of such systems: cooling and trapping techniques allow to control temperature, geometry and dimensionality, while advanced diagnostic techniques provide a direct monitoring of density profiles and momentum distribution, as well as the study of collective and single excitations out of euilibrium. Above all that, the Feshbach resonance phenomenon gives experimentalists also the control of interactions between particles in such systems.
Many reviews provide a detailed description of this phenomenon [30, 23, 31, 32], so in this chapter I will give a syntetic and handle overview of its aspects that are useful for the comprehension of the experimental work I present in this thesis.

2.1 Tunable Interactions in Alkali Atoms

In alkali gases the mean interaction between atoms at long distances is described by the short-range central potential $V(r)$ due to van der Waals forces [33]:

$$V(r) = -\left(\frac{C_6}{r}\right)^6 \tag{2.1}$$

Here the constant C_6 directly define the van der Waal interaction potential range R_0 through the relation:

$$\left(\frac{C_6}{R_0}\right)^6 = \frac{\hbar^2}{mR_0^2} \Longleftrightarrow R_0 = \sqrt[4]{\frac{C_6 m}{\hbar^2}} \tag{2.2}$$

where m indicates the atom mass.
In the ultracold dilute regime, in which these systems are experimentally created and kept, both the mean interparicle distance $r \sim n^{-1/3}$, where n is the mean atom density, and the de Broglie wavelength $\lambda_{dB} = \frac{h}{\sqrt{2\pi m k_B T}}$, with T the temperature of the gas, are much longer than the interaction potential range R_0[1].
These conditions greatly simplify the interaction problem: only two-body collisions matter, and furthermore, at such low energies, atoms never experience the detailed form of $V(r)$. A "far field" approach is then valid, with a scattering wavefunction given at large distances by

$$\Psi_{\mathbf{k}}(\mathbf{r}) = \frac{1}{(2\pi)^{(3/2)}}\left(e^{i\mathbf{k}\cdot\mathbf{r}} + f(\mathbf{k}', \mathbf{k})\frac{e^{ikr}}{r}\right) \tag{2.3}$$

where $\mathbf{k}$ and $\mathbf{k}'$ are respectively the incoming and outcoming wavevectors within the center of mass frame [30].

Provided that the potential is central, the scattering amplitude f can be expressed as a partial wave expansion in terms of wave shifts δ_l, with l =0, 1, 2... the partial wave angular momentum.
Because of the short range character of the van der Waal potential, in the limit of low momenta, phase shifts with $l > 0$ tend to zero [30], and the scattering is predominantly isotropic, i.e. S-wave. A first consequence of this is that collisions between fermions occupying the same quantum state are strongly suppressed due to the Pauli exclusion principle. Furthermore, in the case instead of distinguishable particles or bosons, the scattering amplitude is reduced to the $l = 0$ term:

$$f = -\frac{1}{k\cot\delta_{l=0} + ik} \simeq -\frac{1}{a^{-1} - k^2 r_{eff}/2 + ik} \tag{2.4}$$

Here $\cot\delta_{l=0}$ has been expanded to the second order in k, introducing the *scattering length* a and the *effective potential range* r_{eff}.

It is important to notice that, while a and r_{eff} are in general determined by the microscopic details of the interatomic potential, completely different

[1]In the case of ^6Li R_0 is of the order of $10a_0$ [23], where a_0 is the Bohr radius, while tipical interatomic distances are of the order of 10^2nm.

microscopic interactions can lead to the same low energy expansion of the scattering amplitude (2.4). As a consequence, one can substitute the true potential with a much simpler effective interaction parameterized solely by the two parameters a and r_{eff}, as long as (2.4) is satisfied.
In the regime with $n|r_{eff}|^3 \ll 1$ and $|r_{eff}| \ll |a|$, a very convenient choise is provided by the contact *Fermi pseudopotential* $V_F(r)$ [34, 35, 36], defined by:

$$V_F(r)\Psi(\mathbf{r}) = g\delta^3(r)\frac{\partial_r(r\Psi(\mathbf{r}))}{r\Psi(\mathbf{r})} \tag{2.5}$$

where

$$g = \frac{4\pi\hbar^2 a}{m} \tag{2.6}$$

This choice is equivalent of imposing the *Bethe-Peierls boundary condition* at $r = 0$ [34, 37, 36]

$$\lim_{r\to 0}\frac{\partial_r(r\Psi(\mathbf{r}))}{r\Psi(\mathbf{r})} = -\frac{1}{a} \tag{2.7}$$

From the pseudopotential 2.5 one derives $f_F = -\frac{1}{a^{-1}+ik}$, that is a good approximation of (2.4) for $k|r_{eff}| \ll 1$ [34, 37].
In this case, the entire information on the two-body scattering process is contained solely into one parameter: the S-wave scattering length a.

An important property of the pseudopotential $V_F(r)$ is that it supports one single two-body bound state only if $a > 0$, with energy given by [37]

$$E_b = -\frac{\hbar^2}{\mu a^2} \tag{2.8}$$

with μ the reduced mass. The wavefunction describing this bound state results to be $\Psi_b \propto e^{-r/(2a)}/r$.
This case represent a special and simple case of a general feature of δ_0, and consequently of a, namely its intimate relation with the difference between the energy of the two-atom scattering threshold and the one of a nearby laying bound state supported by the scattering potential. In particular, it is found that $a < 0$ if no bound state lies close to the scattering energy, $a > 0$ if instead a bound state is present. When the bound state becomes perfectly degenerate with the threshold, the phase shift takes the value $\delta_0 = \pi/2$ and a undergoes a divergence[30].

From this general result of scattering theory, we can see that if one could tune the energy difference between the scattering channel and a nearby molecular state, then the value of a could be directly controlled, and with it the whole low-energy collisional properties of an ultracold gas.

In ultracold alkali gases this is physically possible thanks to magnetic *Feshbach resonances*, where the energy of a two-colliding-atoms state (open channel) can be brought to degeneracy with a bound molecular state (closed channel). This can be done via Zeeman effect by tuning an external magnetic field, provided that the two states are characterized by different magnetic moments $\mu_o \neq \mu_c$
In the vicinity of a Feshbach resonance the scattering length exhibits a dispersive behaviour as a function of the applied magnetic field B, that and can be generally parameterized as

$$a(B) = a_{bg}\left(1 - \frac{\Delta B}{B - B_0}\right) \tag{2.9}$$

Here a_{bg} is the off-resonant background scattering length (in absence of coupling to the closed channel), B_0 the magnetic field value at which the resonance is centered, and ΔB describes the resonance width [38, 18].

In general, associated to a Feshbach resonance is an effective range $R^* = -2r_{eff}$, given by [39, 40, 37]

$$R^* = \frac{\hbar^2}{M a_{bg} \Delta B \Delta\mu} \tag{2.10}$$

where $\Delta\mu$ is the magnetic moment difference between the open and closed channels. Provided that $R^* \lesssim R_0$, one can neglect r_{eff} in (2.4), and the resonant scattering can be still described by the pseudopotential (2.5).

^{6}Li, the fermionic isotope of Lithium atoms, represents a powerful system where the scattering length can be finely tuned thanks to three Feshbach resonances characterized by an untypically large magnetic width. The resonances, that occur between each pair of the three internal atomic hyperfine states, are shown in figure 2.1, and their parameters are reported in tabel 2.1 (data from [24]).

Furthermore, thanks to the large width of the Feshbach resonsnces in ^{6}Li, for this Alkali the condition $R^* \lesssim R_0$ is satified, and it is indeed possible to neglect the effect of a non-zero effective range r_{eff} on the parametrization of the pseudopotential and the scattering length [**Petrov2004**].

The tunability of the collision properties is firstly relevant for enhancing the elastic scattering cross section, as given by the optical theorem [30]:

$$\sigma = \frac{4\pi}{k} Im\{f\} \tag{2.11}$$

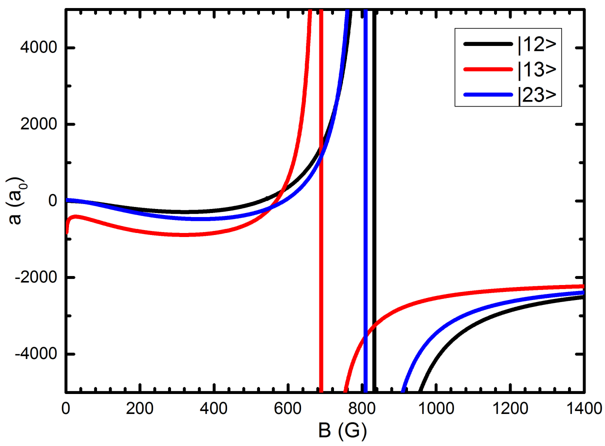

Figure 2.1: Three broad Feshbach resonances among the hyperfine states $|1\rangle$, $|2\rangle$ and $|3\rangle$ in ^{6}Li (Data from [24], supplementary materials).

	B_0 (G)	ΔB (G)	$a_{bg}(a_0)$
$\|12\rangle$	832.18(8)	262.3(3)	-1582(1)
$\|13\rangle$	689.68(8)	166.6(3)	-1770(5)
$\|23\rangle$	809.76(5)	202.2(5)	-1642(5)

Table 2.1: Feshbach resonance parameters for the three lowest hyperfine states $|1\rangle$, $|2\rangle$ and $|3\rangle$ in ^6Li. Data from [24].

This is very useful for achieving an efficient evaporation down to degeneracy temperatures, especially for the present case of Lithium investigated in this thesis.
More fundamentally, Feshbach resonances are a gift of Nature that allows us to explore the many-body physics of complex systems as a function of the interatomic interactions.
In this thesis I have exploited the $|13\rangle$, and expecially the $|12\rangle$, resonances occurring in ^6Li Fermi gas mixtures, to tune the interspecies scattering length throughout the crossover connecting the *Bose-Enstein condensate* (BEC) regime (where $a > 0$), the *unitary limit* ($a = \pm\infty$) and the *Barden-Cooper-Schieffer* (BCS) regime ($a < 0$). The following section gives and overview of these three regimes.

2.2 The BEC-BCS Crossover

Up to now we only presented the energy (2.8) of the two interacting atoms in the case in which they are bound in a molecular state, with $a > 0$. We have yet no clue about the evolution of the total energy of a gas of N interacting fermions, where the two-body scattering lenght is tuned from positive to negative values via a Feshbach resonance.
To gain insight in the matter, let's start with a simple model, involving two fermions confined in a spherical box of radius R, interacting with the contact pseudopotential (2.5). Interestingly, such a simple model qualitatively captures the behaviour of an interacting many-body system, if we regard at the box size as embodying the presence of the N-2 remaining fermions: namely, the hardwall condition at $r = R$ mimicks the effect of Pauli blocking in the limit of low momenta (long wavelenghts) [34].
In this frame, the radius of the box is related to the Fermi wavelength of an ideal Fermi gas with total (spin up and down) particle density $n = n^{\uparrow} + n^{\downarrow}$, given by $k_F = (3\pi^2 n)^{1/3}$, via the definition of the zero-interaction energy [34]

$$E_0 = \frac{\hbar^2}{m}\left(\frac{\pi}{R}\right)^2 \tag{2.12}$$

thus one has [34]

$$R = \left(\frac{5}{3}\right)^{1/2}\frac{\pi}{k_F} \tag{2.13}$$

This model reduces the scattering problem in $r \neq 0$ to the solution of the free Schroedinger equation, with hardwall boundary condition at $r = R$, plus the Bethe-Peirls (2.7) boundary condition at $r = 0$. From this, one can simply derive the eigenfunctions and eigenenergies of the system, obtaining the energy spectrum of the total N-fermion system of fig.2.2 [34]. Only the first two branches are plotted, although discrete higher energy levels are present.

The left side of the plot in fig.2.2 corresponds to magnetic fields below the resonance in fig.2.1 (i.e. at $a > 0$), and the right side to fields above the resonance (i.e. at $a < 0$). As one can see, the lowest energy branch smoothly connects these two limits. Three regimes are defined:

- $k_F a \to 0^+$ (left side). The two fermions are bound in the state with negative energy solution of the two-body problem in free space. The couple find itself in a bosonic molecular state.
- $k_F a \to 0^-$ (right side). This is the case of two weakly attractive fermions with the energy approaching that of the free particle.

- Right on top of the resonance, where a diverges and the particles become strongly interacting, the energy of the system depends only on the box size R. This is the unitary limit, where the features of the system become independent on the scattering wavelength.

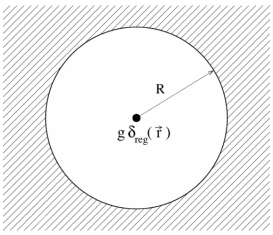

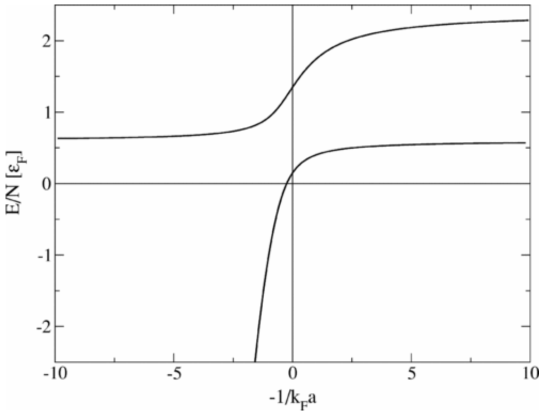

Figure 2.2: Left: sketch of the two-fermions interaction model. $\delta_{reg}(\mathbf{r}) = \delta(\mathbf{r})\partial_r(r\Psi(\mathbf{r}))/r\Psi(\mathbf{r})$ as in 2.5. Right: total energy $E = 1/2N\epsilon$ - with ϵ the fictitious single particle energy- rescaled to the Fermi energy $E_F = \frac{\hbar^2 k_F^2}{2m}$ as a function of $-1/k_F a$. Only the first two branches are plotted. Figure taken from [34].

The upper branch appearing in the spectrum for the two-fermions in a box model corresponds instead to two weakly repulsive single fermions. This is a metastable states of the gas: a three-body collision would lead to the drop of two fermions into the bound dimer state, with the third fermion carrying away the leftover energy and momentum, thus ensuring the conservation laws. This mechanism depupulates the upper branch in favour of the lowest one.

In a more complete treatment for multi-body interaction, the lowest branch in figure 2.2 represent the *BEC-BCS crossover*. Following this branch by means of a Feshbach resonance at T=0, the gas can be adiabatically tuned from a condensate of bosonic molecules, namely the BEC limit $k_F a \to 0^+$, to a superfluid of Cooper pairs in the opposite limit, namely the BCS limit $k_F a \to 0^-$, where one has weakly attractive couples of fermions.
Recalling that the scattering wavefunction in the two-body problem with the contact potential (2.5) takes the form $\Psi_b \propto e^{-r/(2a)}/r$, one finds that the size of the couples is set by a. As a consequence, in the BEC limit $(a/R \ll 1)$

the dimer size is very small with respect to the interparticle distance. On the BCS side, on the contrary, one has $a/R \gg 1$, and thus the size results to be much longer. Close to the resonance, in the unitary limit, the couple size and the mean interparticle distance are of the same order.

The transition throughout these three regimes is pictorially sketched in fig.2.3 in the case of the Feshbach resonance $|12\rangle$ in ^{6}Li.

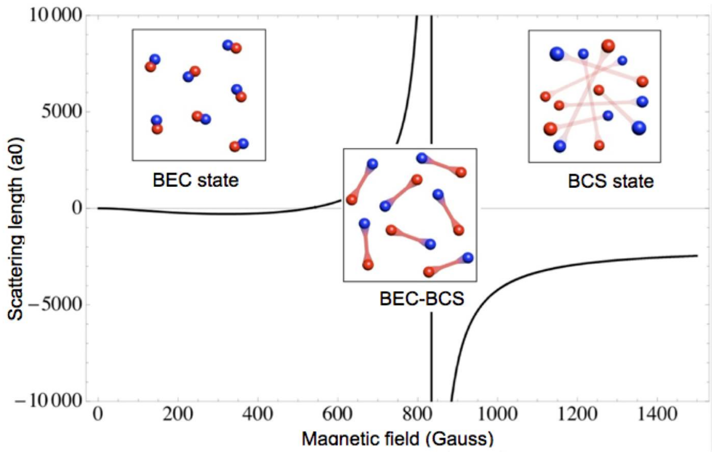

Figure 2.3: BEC, unitary and BCS regime throughout the $|12\rangle$ Feshbach resonance at 832G in ^{6}Li. Colors identify fermions with opposite spin

In principle, the exploitation of a Feshabch resonance to tune the interations would suffer from inelastic scattering: as the gas is cooled down, the Feshbach molecular state is populated via three-body collisions, where a third atom is charged with the binding energy in form of kinetic energy. This process heats up the cloud, leading to atom losses. However these losses do not occur in the lucky case of Lithium-6: here the binding energy on the right side ($a > 0$) of the broad Feshbach resonances is found out to be small enough, so that molecules can efficiently form without severe heating of the cloud. Moreover, further decay via three-body collision to lower lying bound states is suppressed by the Pauli exclusion principle, as two of the three involved fermions are necessarily identical, and they have to approach at $r \sim R_0$. For further details I remind to [38] (chapters 2,5) and to [**Petrov2004**].

To conclude, the broad Feshbach resonances of ^{6}Li allow to explore all the three regimes introduced in this section. With a single physical system it is possible to provide a quantum simulator for the investigation of condensed matter in a widest range of systems -from bosonic superfluids to electrons in superconductors, up to nuclear matter and quark-gluon plasmas thanks to some analogies stimulated in the scientific community by the strongly correlated unitary gas- and in particular to provide an experimental method to study the smooth evolution of one into the other.

Chapter 3

Superfluid Dynamics in a Double-Well

In this thesis I concentrate on the physics of the lower Feshbach branch of the Fermi gas. In particular I study the behaviour of such a state when confined within a double well potential, characterized by a tunable splitting barrier. In this chapter I provide a synthetic but quantitative description of such a system.

3.0.1 Macroscopically Occupied Coherent States

A macroscopically occupied coherent state, either bosonic -as superfluid ^{4}He, BECs of exciton-polaritons in semiconductors- or fermionic -as Cooper pairs in superconductors, superfluid ^{3}He, Fermi atoms interacting via a Feshbach resonance- can be expressed with a scalar complex order parameter

$$\Psi(\mathbf{r}, t) = \Phi(\mathbf{r}, t) e^{i\theta(\mathbf{r}, t)} \tag{3.1}$$

where the global phase $\theta(\mathbf{r}, t)$ ensures the phase coherence of the system and $\Phi(\mathbf{r}, t) = \sqrt{n(\mathbf{r}, t)}$ describes its density profile.
The limit of large particle number N allows one to use mean-field approaches to describe the static and dynamical features of such a state. In the case of bosonic particles the mean-field treatment is based on the Gross-Pitaevskii equation (GPE), namely a non linear Schroedinger equation that accounts for the interactions between particles via an energy term proportional to the local density $n(\mathbf{r}, t)$.
This approach is also suitable in the case of the Lithium system I studied in this thesis, when brought to the limit $k_F a \ll 1$, namely, in the limit of weakely repulsive bosonic dimers on the BEC side of the Feshbach resonance.

With proper extensions that I will explain later on, the GPE approach can be applied also in the strongly interacting regime -the unitary regime-, and beyond the resonance, up to the BCS limit, provided that the composite nature of the bosonic particles is irrelevant.
Let us first summarize the results obtained within the framework of the GPE in the standard situation of the BEC limit: on this side of the Feshbach resonance, each bosonic particle is a molecule composed by two atoms, and the dimer-dimer scattering is governed by a residual interaction. This scattering is mainly elastic and in S-wave; few-body calculations reported in [**Petrov2004**] show that it is described by a scattering length $a_{DD} = 0.6a$

3.1 The BEC Limit

In the case of cold dilute Bose gases, the substitution of real interaction potential with the contact pseudopotential with coupling constant g allows to obtain [41] the time-dependent GPE for the order parameter

$$i\hbar\frac{\partial}{\partial t}\Psi(\mathbf{r},t) = \left(-\frac{\hbar^2\nabla^2}{2M} + V_{ext}(\mathbf{r}) + g_B|\Psi(\mathbf{r},t)|^2\right)\Psi(\mathbf{r},t) \qquad (3.2)$$

In the BEC limit of the Feshbach resonance $g_B = \frac{4\pi\hbar^2 a_{DD}}{M}$, where $a_{DD} = 0.6a$ is the dimer-dimer S-wave scattering length and $M = 2m$ the dimer mass. $V_{ext}(\mathbf{r})$ describes the potential in which the gas is confined. Usually, in ultracold experiments V_{ext} is harmonic:

$$V_{ext}(\mathbf{r}) = \frac{M}{2}(\omega_x^2 x^2 + \omega_y^2 y^2 + \omega_z^2 z^2) \qquad (3.3)$$

The ground state properties, as well as the excitations of the system are derived from the solution of eq.(3.2), and they are summarized in the followig section.

3.1.1 Ground State properties

The ground state wavefunction can be chosen of the form $\Psi(\mathbf{r},t) = \Phi(\mathbf{r})e^{-i\mu_B t/\hbar}$, with a time independent density profile $n(\mathbf{r}) = |\Phi(\mathbf{r})|^2$ and the phase fixed by the chemical potential μ_B. Introducing the wavefunction in eq.(3.2) one obtains the time-independent GPE [41]:

$$\left(-\frac{\hbar^2\nabla^2}{M} + V_{ext}(\mathbf{r}) + g_B|\Phi(\mathbf{r})|^2\right)\Phi(\mathbf{r}) = \mu_B\Phi(\mathbf{r}) \qquad (3.4)$$

For non-interacting particles, (3.4) is the ground state of an harmonic oscillator. Interactions introduce a deviation from its density profile, increasing or decreasing the dimension of the cloud depending whether the interaction potential is repulsive or attractive. In the limit of large $g_B N$ the kinetic energy term $\propto \nabla^2\sqrt{n(\mathbf{r})}$ can be neglected with respect to the interaction term (Thomas-Fermi approximation). Then the density profile $n(\mathbf{r}) = |\Phi(\mathbf{r})|^2$ of the gas takes the form of an inverted parabola:

$$n(\mathbf{r}) = g_B^{-1} Max\{0, [\mu_B - V_{ext}(\mathbf{r})]\} \tag{3.5}$$

From 3.5, the renormalization condition $\int |\Phi|^2 \mathrm{d}\mathbf{r}$=N also provides the explicit form for μ_B [41]:

$$\mu_B = \frac{\hbar\omega_{ho}}{2}\left(\frac{15 N a_{DD}}{a_{ho}}\right)^{2/5} \tag{3.6}$$

where $\omega_{ho} = (\omega_x\omega_y\omega_z)^{1/3}$ is the averaged oscillation frequency, and $a_{ho} = (\hbar/M\omega_{ho})^{1/2}$ the associated harmonic oscillator length.
Moreover, being $\mu = \partial E/\partial N$, from eq.(3.6) one easily derives that the energy per particle in this regime is given by

$$\frac{E}{N} = \frac{5}{7}\mu_B \tag{3.7}$$

The extension of the cloud is given by the Thomas-Fermi radius R_{TF}, that is derivable in the three directions right after (3.6), imposing the condition $\mu = V_{ext}(\mathbf{R}_{TF})$ [41]. Generally, one has that the Thomas-Fermi radius is much longer than the harmonic oscillator length: $R_{TF} \gg a_{ho}$.

The effect of interaction on the cloud extension has consequences on the critical temperature T_c, i.e. the temperature at which the ground state starts being macroscopically occupied: the increase of the cloud size due to repulsive interactions decreases the density, lowering the critical temperature. On the contrary for attractive interactions the density is increased and so is T_c. This effect would be absent in the case of homogeneous gases. The mean-field theory gives the following expression for T_c [42]:

$$T_c = T_0\left(1 - 1.33\frac{a_{DD}}{a_{ho}}N^{1/6}\right); \qquad T_0 = 0.94\frac{\hbar\omega_{ho}}{k_B}(N)^{1/3} \tag{3.8}$$

where T_0 is the critical temperature in the non-interacting limit.

Another important quantity that characterizes the superfluid system is the healing length ξ. This parameter represents a typical length scale derived from the balance between the interaction and the kinetic term in eq.(3.4) [41]:

$$\frac{4\pi\hbar^2 a}{M} = \frac{\hbar^2}{2M\xi^2} \tag{3.9}$$

from which one obtains:

$$\xi = (8\pi n a_{DD})^{-1/2} \tag{3.10}$$

The physical meaning of ξ is the minimum distance over which the oreder parameter can heal. This quantity is relevant in superfluid effects, as it gives an estimate of the coherence length of the system.

3.1.2 Dynamical properties

When the system is not at equilibrium, superfluid dynamics will occur, described by the time dependent GPE (3.2) for the total wavefunction $\Psi(\mathbf{r}, t)$. For small deviations of the wavefunction from its form at equilibrium, given by (3.4), one can impose solutions of eq.(3.2) in the form of small oscillations of the order parameter with frequency ω. In a uniform gas, the oscillation amplitudes are plane waves, and the dispersion relation $\omega(\mathbf{q})$ takes the Bogoliubov form [41]:

$$\hbar\omega(\mathbf{q}) = \sqrt{\frac{\hbar^2 q^2}{2M}\left(\frac{\hbar^2 q^2}{2M} + 2gn\right)} \tag{3.11}$$

where $\mathbf{q}$ is the wavevector of the collective excitation. The Bogoliubov spectrum is linear at low momentum, yelding the phonon dispersion $\omega = v_c q$, being $v_c = \sqrt{gn/M}$ the sound velocity. At higher momenta the spectrum evolves into the one of the free particle, $\sim p^2/(2M)$.

In the case of harmonic trapping, the continuous dispersion become descrete (with $\mathbf{q}$ the index of quantization). However, one can show that the dispersion is again phononic at low momenta in the limit of large N[41].

Among all the collective oscillations exhibited by trapped gases, particular attention must be paid to the motion of the center of mass of the system: this oscillation is decoupled from the internal degrees of freedom, and is solely characterized in each direction by the frequencies of the harmonic trap. The motion of the center of mass is referred to as dipole oscillation.

In addition to phononic vibrations, the dynamics of macroscopic bosonic systems cooled down to temperature below T_c is characterized by the appearence of superfluidity. Superfluidity shows up with the absence of viscosity, the reduction of the moment of inertia, and new collective phenomena, such as the presence of persistent currents, quantized vortices, second sound. Superfluid motion is described by a velocity fixed by the phase of the order parameter, following the derivation of the quantum particle current density $\mathbf{J} = n\mathbf{v}_s$ [41, 8]:

$$\mathbf{J}(\mathbf{r}, t) = \frac{\hbar}{2iM}(\Psi^*\nabla\Psi - \Psi\nabla\Psi^*) \implies \mathbf{v}_s(\mathbf{r}, t) = \frac{\hbar}{M}\nabla\theta(\mathbf{r}, t) \tag{3.12}$$

Introducing the expression for $\mathbf{v}_s$ in eq.(3.2) within the Thomas-Fermi approximation, the equation takes the form of the Euler equation for an ideal irrotational fluid [41]. This interpretation of the absence of viscosity was firstly proposed by Landau for superfluid ^{4}He: he described it as a two-component system, where an inviscid irrotational fluid with velocity $\mathbf{v}_s(\mathbf{r}, t) = \frac{\hbar}{M}\nabla\theta(\mathbf{r}, t)$ cohexists with a normal fluid. In this vision the transition from the superfluid componet to the normal, viscous one is explained with a sharp excitation energy spectrum as the phononic one in eq.(3.11). The linear behaviour of the Bogoliubov spectrum at low momenta implies that the relative motion of an object within the superfluid can exchange energy with it only if its velocity is $v > v_c$. If instead $v < v_c$ the superfluid is not excited, and the relative flow is persistent without viscosity.[8]

Higher order excitations in a superfluid may appear as a topological defect in the density profile: it can be shown that a zero-density point in the superfluid is equivalent to the presence of a phase slippage in the order parameter [8, 19], leading to the appearence a soliton in 1D systems, or of a superfluid vortex in 2D and 3D. One usually refers to the vortices as quantized vortices, because the circuitation of the superfluid velocity, eq.(3.12), in a closed path enclosing the topological defect -namely the filament core of the vortex- takes quantized values [8]. As we will see later on, solitons and vortices are responsible of dissipation phenomena in excited superfluids.

To complete this overview on the dynamics of a coherent system, I emphasize the point that, even if the transition to a Bose-Einstein condensate ensures the existence of a scalar order parameter, hence the occurrence of superfluidity, the superfluid state and the BEC state are not equivalent: in a superfluid only a percentage of particles is condensed in the ground state. Penrose and Onsager have derived that in ^{4}He the condensed fraction remains $\sim 8\%$ down to absolute 0 temperature under its own vapour pressure, owing to strong interparticle collisions [8].

3.2 Extension of the Mean-Field GPE to the Unitary Gas and the BCS Limit

The scenario depicted in the previous section is qualitatively and quantitatively affected by strong interactions when the system is brought towards and beyond the resonance.

The evolution towards the crossover can be taken into account in the GPE via proper parametrization of the interaction term in eq.(3.4) and (3.2), thus through a renormalization of the coupling constant g. Many different approaches exist in literature, using an expansion in a of the interaction term derived both for a weakly repulsive BEC [20] or for a weakly actractive Fermi gas [43] [27].
Such a parametrization procedure can be based either on quantitatively correct Monte Carlo data [25], or on mean-field results on the BEC-BCS crossover based on the solution of Bogoliubov-de Gennes (BDG) equations [17].
Here I will only focus on the fact that the resulting GPE, usually referred to as modified GPE, yields a quantitatively correct description of the static features of the system throughout the whole BEC-BCS crossover. However, while moving from the BEC to the BCS limit, it will fail both quantitatively and qualitatively to describe the superfluid dynamics, beyond a certain value of the interaction parameter $k_F a$. The failure is due to the progressive reduction of the binding energy of the atom pairs moving towards the BCS side of the Feshbach resonance (see again the trend of the lowest branch in the simple model spectrum in figure 2.2). Namely, when the pairing gap energy becomes of the same order of magnitude of the collective excitations of the Feshbach collective mode, and the pair-breaking effect can become noticeable.
In other words, for $1/(k_F a) \gtrsim 0$ and $1/(k_F a) < 0$, the condensed fraction in the superfluid is no longer equal to 100% and reduces moving towards the resonance. This lead to a contamination of the collective mode with the continuum of single-fermionic excitation. The merging of the branch into the continuum has been theoretically studied in [44].
It is worth bringing into focus that this has profound effect on the critical velocities in the superfluid: on the BEC side the critical velocity is set by

the phononic dispersion, while on the BCS side the upper limit is given by the pair-breaking process.
The modified GPE cannot account for the non-condensed fraction of the superfluid and its effect on the complessive dynamics of the system, because it treats the superfluid pairs as elementary bosonic particles, without accounting for the fermionic degrees of freedom, for which more involved theoretical approaches are needed [17, 44]. I will show in the following how the modified GPE quantitatively and qualitatively fails [44, 45, 22] in predicting the critical velocities in the superfluid as a function of the interaction strength parameter $1/(k_F a)$.

In the unitary limit and the BCS regime, a qualitatively correct description of the dynamics of the superfluid is provided by the mean-field BDG theory, that is based on a spinorial equation for a two-component dilute superfluid of fermions [27]: in these equations the diagonal elements of the hamiltonian matrix correspond to the non-interacting Hamiltonian of a Fermi gas in a trap potential, while the off-diagonal terms accounts for the coupling between the tho spinorial components.
At present there is however no self-consistent theory approach able to describe the whole crossover, despite recent progresses have been done in this frame: in [46] a time dipendent spinorial equation has been proposed that includes additional terms in the diagonal matrix element of the BDG equation.

Due to its conceptual simplicity, I will base on the modified GPE theory to outline the variuos dynamical regimes expected for the superfluid within a double well potential.

3.3 Superfluid Dynamics within a Double Well Potential

In order to capture the qualitative features of a superfluid evolving in a double well configuration, as the one employed in our experimental setup, it is instructive to start considering the dynamics of a BEC of a weakly interacting dimers in a 3D harmonic trap splitted in two reservoirs by a Gaussian barrier. Namely, let's consider eq.(3.2) with V_{ext} given by

$$V_{ext} = V_{ho} + V_{barr} = \frac{1}{2} M \sum_i \omega_i^2 x_i^2 + V_0 e^{\left(\frac{-2z^2}{W_z^2}\right)} \tag{3.13}$$

where W_z is the $1/e$ size of the barrier along the trap axial direction z. Along the trasverse directions the barrier is considered infinitely extended, with fixed width.

On general grounds one can discriminate two different dynamical regimes depending on the heigh of the barrier V_0 with respect to the chemical potential μ_B given by (3.6): a hydrodynamic regime, when $V_0 \ll \mu$, and a tunneling regime, for $V_0 \gtrsim \mu$
In the following I will give a syntetic overview of these two dynamical phases.

3.3.1 Hydrodynamic regime

In the hydrodynamic regime one has $V_0 \ll \mu$. In this situation the barrier can be regarded as a small defect experienced by the BEC while moving within the harmonic potential. Reference [47] presents a numerical calculation for a dilute BEC oscillating in a cigar-shaped trap in presence of a single localized gaussian scatterer with $V_0/\mu = 0.24$, for different superfluid velocities: it is obtained that for velocities much smaller than the critical sound velocity $v_c = \sqrt{gn/M}$ derived from (3.11), the defect causes the presence of a stable dip -namely a soliton in a 1D model- in the density profile pinned into the barrier region, while the motion is affected only via phonon excitations. This results in a renormalization of the dipole oscillation frequency ω_z^0 in absence of barrier:

$$\frac{\delta\omega_z}{\omega_z^0} = -\sqrt{M\pi}\frac{3V_0\xi}{8\mu^{3/2}}\omega_z^0 \tag{3.14}$$

Here ξ is the healing length relative to the central density. The result is a typical feature of the superfluid, with no energy dissipation and thus no damping of the dipole oscillation.

By increasing the relative velocity between superfluid and barrier one may enter a dissipative regime, where the density profile is perturbed throughout the whole condensate and a damping of the oscillation amplitude is observed in time. This behaviour is associated with a detachment of the topological defect from the low density region in proximity of the barrier, and the consequent propagation of the defect in the form of solitons in 1D, vortices in 3D-, throughout the superfluid.

The same picture holds in the unitary and BCS regime [48], except for the qualitative (and quantitative) change in the critical velocity, that beyond the resonance is set by the pair-breaking effect. This change has been theoretically studied in the case of $V_0 \ll \mu$ in [19, 43, 22], and experimentally observed in [45].

3.3.2 Tunneling Regime

This regime occurs when the barrier potential height becomes comparable or heigher than the chemical potential. In this configuration the superfluid particles can oscillate across the barrier only through tunneling processes, because their energy is too low to classically pass over it. Here, the overall system can be modelled as two reservoirs, each containing a superfluid system, weakly linked via a non-zero coupling through the barrier.
The dynamics of the superfluid exhibits different features depending on the parameters of the system. In particular one can identify three sub-cases determined by the competition between the interaction and the kinetic terms in the GPE. Also the size of the barrier plays a role and must be compared with the healing length of the superfluid.
The three sub-regimes are nicely captured by the so called two-mode approximation [49]. This simple model assumes that the total wavefuntion can be expressed as a composition of the two overlapping single-well wavefunctions:

$$\Psi(\mathbf{r},t) = \Psi_1(\mathbf{r},t) + \Psi_2(\mathbf{r},t) = \Phi_1(\mathbf{r})\phi_1(t) + \Phi_2(\mathbf{r})\phi_2(t) \tag{3.15}$$

where $\Phi_i(\mathbf{r})$ are spatial wavefunctions describing the density profile of the two localized states, while $\phi_i(t)$ are time dependent order parameters of the form

$$\phi_i(t) = \sqrt{N_i(t)}e^{i\theta_i(t)} \tag{3.16}$$

It is very important to note that the spatial and the time dependence are decoupled in (3.15). The physical meaning of the factorization is that the two-mode approximation assumes that the single-well state is not perturbed in its shape while the number of atoms N_i in each well evolves in time, together with the associated phase θ_i

Inserting (3.15) in the non-modified time-independent GPE (3.4), where the external potential is now given by (3.13), one obtains the following equations for the two time-dependent order parameters $\phi_i(t) = \sqrt{N_i(t)}e^{i\theta_i(t)}$ [9]:

$$i\hbar\frac{\partial \phi_1}{\partial t} = (E_1^0 + U_1N_1)\phi_1 - K\phi_2 \tag{3.17a}$$

$$i\hbar\frac{\partial \phi_2}{\partial t} = (E_2^0 + U_2N_2)\phi_2 - K\phi_1 \tag{3.17b}$$

with the following expression for the parameters [9]:

$$E_i^0 = \int \left[\frac{\hbar^2}{2M} |\nabla \Phi_i|^2 + \Phi_i^2 V_{ext} \right] \mathrm{d}\mathbf{r} \tag{3.18a}$$

$$U_i = g \int \Phi_i^4 \mathrm{d}\mathbf{r} \tag{3.18b}$$

$$K = \int \left[\frac{\hbar^2}{2M} (\nabla \Phi_1 \nabla \Phi_2) + \Phi_1 \Phi_2 V_{ext} \right] \mathrm{d}\mathbf{r} \tag{3.18c}$$

Here E_i^0 are the zero-point energies for each localized state; U_i are the on-site interaction energies related again to the single states Φ_i; K is the coupling matrix element [9].

In our experimental configuration the trap potential is chosen symmetrical with respect to the barrier. This means that the two localized spatial wavefunctions are equivalent: $\Phi_1(\mathbf{r}) = \Phi_2(\mathbf{r}) = \Phi(\mathbf{r})$.
This also means that $E_1^0 = E_2^0$ and that $U_1 = U_2 = U$.
Moreover, one can show through a basis transformation $(\Phi_1; \Phi_2) \rightarrow (\Phi_s; \Phi_a)$ [50, 27] that K is proportional to the difference $E_- - E_+$ between the lowest stationary symmetric and antisymmetric many-body states, solutions for the double well potential when the number of atoms is equally distributed $(N_1 = N_2 = N/2)$.

Defining the population imbalance $z(t) = \frac{N_1(t) - N_2(t)}{N}$ and the phase difference $\theta(t) = \theta_1(t) - \theta_2(t)$ between the two wells, one can linearize eq.(3.18) and obtain two coupled equations for $z(t)$ and $\theta(t)$ [9]:

$$\dot{z} = -\sqrt{1 - z^2} \sin\theta \tag{3.19a}$$

$$\dot{\theta} = \Lambda z + \frac{z}{\sqrt{1 - z^2}} \cos\theta \tag{3.19b}$$

where the time has ben rescaled as $2Kt/\hbar \rightarrow t$, and $\Lambda = NU/(2K)$.

It is clear from equations (3.19) that if initial conditions $z_0 \neq 0$ or $\theta_0 \neq 0$ are set, namely if one initializes the system in an unbalanced configuration, where an energy difference exists between the total left and right single-well wavefunctions $\Psi_1(\mathbf{r}, 0) = \Phi_1(\mathbf{r})\phi_1(0)$ and $\Psi_2(\mathbf{r}, 0) = \Phi_2(\mathbf{r})\phi_2(0)$, then an oscillatory atom current $I = \dot{z}N/2$ is observed throughout the barrier.

z and θ can be interpreted as two canonically coniugated variables [9, 50, 8], satisfying the relations $\dot{z} = -\frac{\partial H}{\partial \theta}$, $\dot{\theta} = \frac{\partial H}{\partial z}$ with the Hamiltonian

$$H = \frac{\Lambda}{2} z^2 - \sqrt{1 - z^2} \cos\theta \tag{3.20}$$

In a simple mechanical analogy, H describes a non-rigid pendulum, of tilt angle θ and angular momentum z.

It is worth noticing that the parameters describing the barrier enter the equations not only in in a direct way in K, via the external potential V_{ext}, but also, and more influencing, into the shape itself of the two spatial functions $\Phi_{1;2}(\mathbf{r})$. Let's stress in fact that the choice of these functions has to yield from the minimization of the single localized state energy. The result is that the higher and the thicker is the barrier, the more localized will result $\Phi_{1;2}(\mathbf{r})$. Consequently the coupling between the two superfluids decreases, and $\Lambda \to \infty$. On the contrary, if the barrier is low and thin, the coupling increases, and $\Lambda \to 0$. In essence, one can identify the three sub-regimes depending on the balance between the interaction term and the tunneling term, namely on $\Lambda = NU/(2K)$. These three regimes are presented in the following.

Rabi regime

In the limit $\Lambda \ll 1$, i.e. in the case of strong coupling between the two reservoires, equations (3.19) yield the Rabi oscillation frequency for the atom current [9]

$$\omega_R = \frac{2K}{\hbar} \tag{3.21}$$

It is worth stressing the fact that if one imagines to increase the barrier height V_0, the frequency (3.21) is expected to decrease, as a consequence of the more localization of the two superfluids within the singe wells.
On the opposite, decreasing the barrier height, this regimes smoothly merges into the hydrodynamic regime, when the barrier height is lowered down to $V_0 < \mu$. In this limit the frequency tends to match the dipole oscillation frequency as stated by 3.14.

Josephson regime

If $\Lambda \sim 1$, the two variables z and θ result coupled as from (3.19).
If a small initial imbalance $z_0 \ll 1$ is set, one can approximate eq.(3.19) for small oscillation amplitudes, yielding the linear equations [9]:

$$\dot{z} \simeq -\theta \tag{3.22a}$$

$$\dot{\theta} \simeq (\Lambda + 1) z \tag{3.22b}$$

These are sinusoidal oscillations with a frequency

$$\omega_J = \frac{1}{\hbar}\sqrt{2UNK + 4K^2} \tag{3.23}$$

This frequency is usually referred to as plasma frequency.
Again if the height of the barrier is increased, the plasma frequency is expected to decrease.

In essence, in a system of two superfluids coupled by a link weak enough to allow a considerable overlap, but still high enough to allow a balance between the self-interaction term and the tunneling one, a sinusoidal particle current is observed in absence of external forces. This behaviour is not specific for a superfluid in a double potential well: such oscillations are found in many other systems, varying from liquid He to superconductors, and the phenomenon is nowadays denoted as Josephson effect. A noteworthy example is that of a superconductor junction, where an applied voltage drop results in an oscillating current. This effect was first predicted by Josephson in 1962 [5] and experimentally observed few months later by Anderson and Rowell [51]. It is worth noticing that in the case of a superconductor junction, the energy difference between the two states introduced by the two-mode approximation is not due to an initial population imbalance z_0, but to the presence of a term $\Delta E = E_1^0 - E_2^0$ in the equations (3.19), proportional to the applied voltage drop. In our case this term is zero because of the trap symmetry.

In a very simple picture, the appearence of macroscopic coherent effects in superconductors, as the Josephson effect or the presence of persistent non-dissipative currets itself, is due to the condensation of the Bose-like Cooper pairs predicted by the BCS theory [38]. I have already introduced the BCS theory in chapter 2 to describe the state of a Fermi atom gas beyond the Feschbach resonance. In fact, the BCS theory predicts that coupled electrons remain only weakly attractive, and the theory associates to the Cooper pairs a dimension that is much bigger than the typical interparticle distance: from this point of view the limit $1/(k_F a) \to -\infty$ in a Feshbach resonance has many analogies with the superconductor electron state.

Non-linear and self-trapping regime

Within a certain parameter range, a numerical solution [9] of the full equations (3.19) might lead to non-sinusoidal oscillations that represent the anharmonic generalization of the Josephson regime.
In particular, in the limit of $\Lambda \gg 1$, namely for large non-linear interaction

effects, a novel dynamical regime is predicted from the study of equations (3.19): a macroscopic quantum self trapping phase [9]. In this case, $z(t)$ ceases to oscillate around zero, and presents fast oscillations of small amplitude around a mean value $\langle z \rangle \sim z_0 \neq 0$.
Figure 3.1 [9] shows solutions for initial values $z_0 = 0.6, \theta_0 = 0$ and for increasing values of Λ. The anarmonicity effect is evident. In the last panel d) of 3.1 the system undergoes a critical transition at $\Lambda = \Lambda_c = 10$: for higher values the population imbalance presents small fast oscillations around $\langle z(t) \rangle \neq 0$. In the non-rigid pendulum analogy, this corresponds to an initial angular momentum z_0 sufficiently large to swing the pendulum over the $\theta = \pi$ vertical orientation. The non-zero mean value of the population imbalance -the momentum- corresponds to a perpetual rotatory motion.
The critical value Λ_c above which this behaviour is shown, can be derived from the condition

$$H(0) = \frac{\Lambda}{2} z(0)^2 - \sqrt{1 - z(0)^2} \cos\theta(0) > 1 \tag{3.24}$$

yelding

$$\Lambda_c = 2 \left(\frac{\sqrt{1 - z(0)^2} \cos\theta(0) + 1}{z(0)^2} \right) \tag{3.25}$$

From (3.25) emerges that, for fixed interaction and barrier parameter, thus for fixed values of U, K, Λ, the self trapping regime is reached by increasing the initial population imbalance z_0 (thus reducing Λ_c).

The full dynamic behaviour of eq.(3.19) is depicted in plot 3.2 [9], that shows the $z - \theta$ trajectories at constant energies. In particular the closed trajectories desribe the oscillation linear and non-linear Josephson dynamics, while the open trajectories correspond to the self-trapping regime, where is nearly fixed around $\langle z(t) \rangle \neq 0$ and the phase difference continues running from $-\pi$ to π with a nearly linear trend, as stated by the limit of constant $z = z_{st}$ for equations (3.19). The result is a sow-tooth curve $\theta(t)$, with jumps back to $-\pi$ whenever the phase reaches the maximum value π.

Within the two-mode approximation the system dynamics is almost frozen once entered the self-trapping regime, with open trajectories in the $z - \theta$ plane as in fig.3.2. This is nicely seen in the frame of Bose-Hubbard treatment in second quantization formalism [50, 52] for a superfluid in a double well potential: this model derives an energy spectrum of the Hamiltonian (3.20) with time-constant parameters U, K, Λ, namely assuming the two-mode approximation. The spectrum presents eigenstates with increasing energy as a

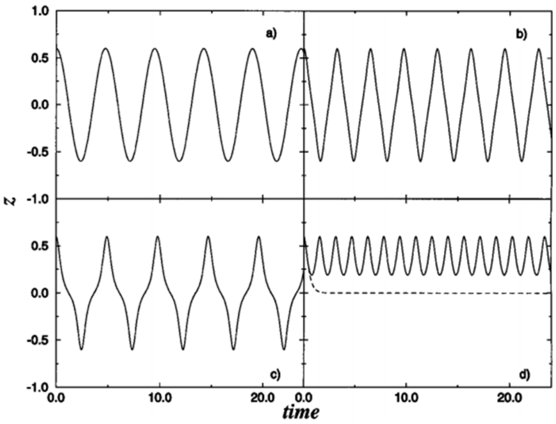

Figure 3.1: $z(t)$ vs rescaled time, for $z_0 = 0.6, \theta_0 = 0$ and a) $\Lambda = 1$, b) $\Lambda = 8$, c) $\Lambda = 9.9$, d) $\Lambda = 10$ (dashed line) and $\Lambda = 1$ (solid line). Figure taken from[9]..

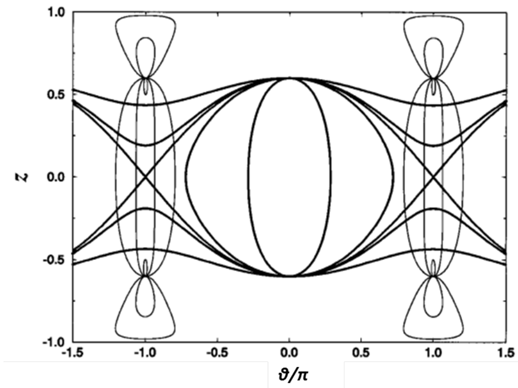

Figure 3.2: $z(t)$ vs $\theta(t)$. Bold lines: $z_0 = 0.6, \theta_0 = 0$, Λ=1, 8, 10, 11, 20. Other lines: $z_0 = 0.6, \theta_0 = \pi$, Λ=0, 1, 1.2, 1.5, 2. Figure taken from [9].

function of the initial population imbalance. The work [52] derives the occupation probability of these levels, obtaining that the self-trapping regime is described by the occupation of doublets of high energy levels with vanishing energy split. A small Franck-Condom overlap between two consecutive doublets yields the small amplitude oscillation of the population imbalance, while the energy spacing between the doubltes determines the fast frequency of the oscillation.
From eq.(3.19(b)), neglecting the second term on the right since $\Lambda \gg 1$, one can easily see that the sowtooth frequency is $\nu_{st} = z_{st} NU/\hbar$, namely $\nu_{st} \sim (\mu_1 - \mu_2)/\hbar$, where I introduced the chemical potential difference between the two localized states in the self-trapping regime [52].

The self-trapping regime is a tipical feature of atomic superfluid gases and polariton systems, while it is neither observable in superconductor junctions nor in superfluid He. For the first case, this is due to the fact that the pairing gap associated to the electron Cooper pairs is very small with respect to the energies involved in the Josephson dynamics: an increase of the voltage drop would lead to pair breaking before reaching the self-trapping critical value. For the case of He systems it is pratically impossible to access the tunneling regime, and dissipation phenomena prevent the osservation of the macroscopic quantum self-trapping, as I will explain in the following.

3.3.3 Beyond the Two-Mode Approximation: Dissipative Effects

This scenario is further enriched both in multi-mode systems, i.e. when the energy difference $\delta\mu$ can exceed the radial degrees of freedom [28], and in systems where the quantum fluctuations associated with the two superfluid wavefunctions $\Psi_{1,2}(\mathbf{r}, t)$ are non negligible [10]. In both cases the two-mode approximation ends to hold. It is in fact no longer possible to assume that the spatial dependence of the two density profiles $\Phi_{1,2}(\mathbf{r})$ remains constant in time, irrespective of the evolution of the number of atoms that are oscillating throughout the barrier.

Within this frame it is very important to remember that a phase difference $\theta = \pi$, namely a phase slippage, is equivalent to the formation of a topological defect in the superfluid density profile (a soliton in 1D, a vortex in 2D and 3D).
The self trapping-regime of a multi-mode system is expected to become unstable against dissipation of energy induced by the detachment of these topological defects from the barrier, and their propagation into the superfluid bulk. [28, 46, 53].
In simple words, the propagations of excitations within the superfluid allows the system to dissipate its energy and the condition 3.24 ends to hold. The system does not enter the self-trapping regime, while its dynamics evolves in more complex phenomena.
A well known example is that of superfluid Helium, where phase slips have been observed in many experiments since the first of Richards and Anderson in 1965. In these experiments the weak link between the two superfluid He reservoires is created by small orifices. An applied pressure difference mimics the voltage drop in superconductors, or a non-zero initial imbalance in our

configuration. Again an oscillating atom flow is observed as a consequence of the applied pressure difference. The phase slips manifest as sharp non-linearities in the response of the oscillation amplitude as a function of the pressure difference[8, 15, 54], and lead to the formation of higher order excitation such as vortices in the two superfluid bulks.

3.3.4 Failure of the Modified GPE

The mathematical derivation for the coherent dynamics within a double well that I have presented above is yield from the non-modified GPE equation (3.4), thus it is in principle valid only on the BEC side of the Feschbach resonance. As already said, an extension of this treatment is obtained by the modified GPE theory under proper renormalization of the coupling constant. However, the modified GPE fails in recovering the dynamical feature of the system connected with contamination of the collective mode with the single excited fermionic states, as explained in section 3.2.
A better approach would be given by the Bogoliubov-de Gennes theory. Unfortunately, a rigourous derivation of the Josephson equations (3.18), (3.19) from the BdG within a two-mode approximation is not available. Nonetheless, the theoretical work [27] shows that the effects on the oscillating current velocities due to the pair breaking can be accounted for via a renormalization of the parameters U and K, deriving them from the stationary solution of the BdG equation.

The qualitative failure of the GPE on the crossover and BCS side is apparent in the plot 3.3 [43], that presents a comparison between the maximum amplitude of the Josephson current in presence of a square barrier at various barrier heights, derived from the BdG theory (symbols).
The maximum current $I_0 = NK/\hbar$ (derived from (3.19) in usual time units) is expected to never exceed the upward limit set by the critical velocities in the superfluid. On the BEC side the critical velocity is given by the sound velocity v_c, that increases as one moves toward the crossover. However on the BCS side the critical velocity is set by the pair breaking and $v_{pb} < v_c$. The trend of v_{pb} is shown by the solid line and is derivable from the BdG theory. The matching point between the two branches occurs at the unitary limit.
Fig. 3.3 shows that the GPE adequately describes the maximum current to be always lower than the critical value on the BEC limit (notice that the upper dashed line corresponds to a barrier value of $V_0/E_f = 0.025$, that means that the curve is actually approching the ideal maximum current in the su-

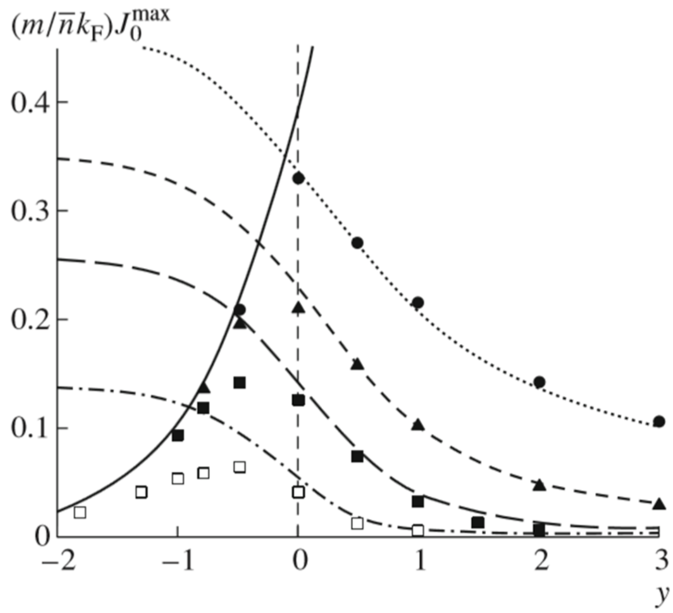

Figure 3.3: Maximum Josephson current obtained with a modified GPE (dashed lines) versus $y = 1/(k_F a)$ for different values of the barrier heigh: V_0/E_F=0.025 (dotted), 0.1 (short dashed), 0.2 (dashed), 0.4 (dashed-dotted). The square barrier size is $L = 4/k_F$. The critical current set by pair breaking is also plotted (solid line). The results are compared with the maximum Josephon current obtained in [19] (symbols) from BdG calculations. Graph from [43].

perfluid without barriers); on the BCS side instead the GPE theory leads to an increasing value of I_0, while the pair breaking effect whould imply an opposite decreasing behaviour.

In plot the dashed lines for the GPE are also compared to the theoretical results obtained by [19] (dotted data), where I_0 is obtained from BdG density profiles $n(\mathbf{r})$. The results from[19] are in agreement with the presence of an upper velocity, both in the BEC side and in the BCS side.

Chapter 4

Experimental Setup and Procedure

In this chapter I will give an overview of the experimental setup and procedures necessary to create a BEC-BCS crossover superfluid in a double well potential, and that allowed me to perform the first characterization of such systems in the Lithium lab.

In particular I will focus on the new parts of the apparatus which were developed with my direct engagement during the period of this thesis: a thin optical barrier focalization on the atom cloud and its characterization.

A detailed description of the other pre-existing fundamental parts of the apparatus, can be found in the Master thesis [55] and [56].

The protocols employed for preparing the superfluid sample are well established thanks to the previous works [57][58]. Section 4.1 of this chapter is dedicated to the summariration of these protocols.

4.1 Preparation of a Superfluid Fermi Gas

I summarize here the main steps that build up the preparation procedure of the degenerate gas at the desired Feshbach field in the vacuum chamber. The procedure comprehends a first cooling by means of interaction of atoms with D2 and D1 light, exploiting the transitions shown in figure 4.1, the transfer of atoms in the optical dipole trap, and a second evaporative cooling within the trap.

Laser cooling stage

The experimental sequence starts with loading the MOT operating on the transition D2 ($2S_{1/2} \rightarrow 2P_{3/2}$). The MOT light configuration consists of three

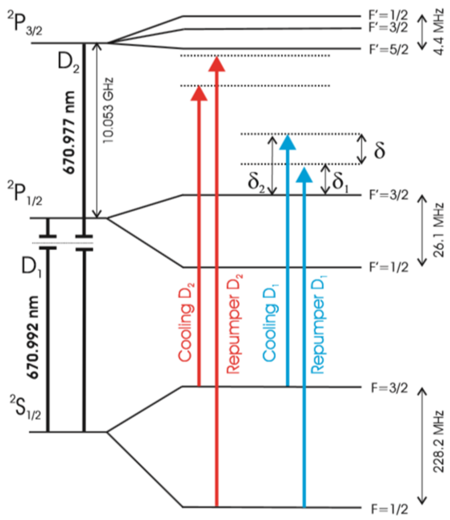

Figure 4.1: D2 and D1 transition in ^{6}Li. Figure from [57].

Parameters	experimentally optimized values
I	$7 \times I_S = 7 \times 2.54$ mW/cm$_2$
$\frac{I_R}{I_C}$	2:3
δ_C	-9Γ
δ_R	-6Γ
T_f	2.5 mK

Table 4.1: Optimized parameter for the D2 laser cooling stage.

retro-reflexed beams -with radius of about 1.5 cm- containing both cooling and repumping light. Parameters have been experimentally optimized to maximize the number of trapped atoms. Where I_S is the saturation intensity of the D2 transition, the label C and R refer respectively to the cooling and repumper beam.T_f indicates the reached temperature.
A second step is carried out by reducing in modulus the detunig of both cooling and repumper light and simultaneously reducing their intensity to about $\sim \%1$ of the original value, in order to compensate the increase of photon scattering rate, that would lead to atoms loss: We end up with a total number of collected atoms $N_0 \sim 1.6 \times 10^9$ at 500 μK. This temperature is significantly higher than the Doppler limited one ($\sim$ 150 μK) due to unresolving of the hyperfine levels in the D2 line. To overcome this limitation a further laser cooling technique on the D1 line ($2S_{1/2} \rightarrow 2P_{1/2}$) has been succesfully developed in this lab [57, 58]. Thanks to a combination of Sisyphus cooling

Parameters	experimentally optimized values
I	$\frac{7}{100} \times I_S = 7 \times 2.54$ mW/cm^2
$\frac{I_R}{I_C}$	2:3
δ_C	-3Γ
δ_R	-3Γ
T_1	500 μK

Table 4.2: Optimized parameter for the D2 laser cooling stage.

Parameters	experimentally optimized values
I	$2.7 \times I_S = 2.7 \times 2.54$ mW/cm$_2$
$\frac{I_C}{I_R}$	0.2
δ	-0.2Γ
δ_C	5.4Γ
δ_R	5.2Γ
T_f	~ 135 μK

Table 4.3: Optimal parameters for D1 cooling.

and velocity selective coherent population trapping, the D1 cooling technique allows to reduce the temperature of the cloud down to ~ 40 μK with no significant atom losses and a factor of 20 gain in the phase-space density. In table 4.3 the optimized experimental parameters for D1 cooling are reported.

Thanks to intensity imbalance between repumper and cooling light, a significant fraction of atoms ($\sim 85\%$) is already found in the $F = 1/2$ manyfold, which is the one exploited for evaporative cooling.

ODT loading

The optical dipole trap (ODT) is ramped up over 5 ms during the D2 cooling stage and it is fully on by the time the D1 phase is applied; it is constitued by two crossed laser beams, in order to assure 3D confinement.
The first laser beam is generated by a 200 W multimode ytterbium fiber laser (IPG LASER) with a central wavelength of 1073 nm and with almost a 3 nm broadening, whose initial power is set at 120 W.
The beam in out of the laser is collimated with waist ~ 1 mm onto an AOM and afterwards brought to the science chamber and focused onto the atoms with a waist of 45 μm both in the x and y direction.

The power stabilization of IPG is achieved by means of the AOM, controlled by a a PID circuit, which recieves the feedback signal from a pick-up beam shined onto a linear photodiode.

At full power the ODT has a depth of about 3 mK, sufficient to trap atoms from the laser cooling stage. To optimize the transfer from into the ODT, we increase the trapping volume of the ODT by appling a fast sinusoidal modulation to both the central frequency and the amplitude of the IPG's AOM. The frequency modulation (FM) changes the frequency of oscillation of the AOM piezoelectric (pzt) trasducer; this results in a displacement of the position of the focused beam in the science chamber. The frequency of this modulation is 600 kHz, much greater than the trapping frequencies, and atoms experience a time-averaged dipole potential with an effective waist larger than the one without modulation ($\sim 100\mu$m).
The profile of the time-averaged potential is non-Gaussian: the distorsion is corrected by the amplitude modulation (AM), with frequency twice the FM frequency and a relative phase of $\pi/2$.

In addition to the IPG beam, a second optical trap beam, crossing the IGP with an angle of $\sim 14°$ is shined onto the atoms.
This second beam is produced by a monolithic Nd:YAG NPRO (Non-Planar Ring Oscillator) laser (Mephisto) with central line at 1064 nm. The output of the laser is coupled in a polarization maintaining fiber to bring it in proximity of the vacuum chamber and afterwards focalized onto it. The waist of the beam is cilindrically symmetric, with a value of 45 μm in the trap focus. The initial power of the Mephisto beam is set at 2 W. The Mephisto beam provides additional trapping confinement once the IPG light is significantly reduced during evaporation.

The total number of atoms transferred into the ODT is $\sim 2 \times 10^7$, that is actually of two order of magnitude less than the initial collected atoms in the MOT. As already reported in the previous paragraph, the temperature of the sample is $T \gtrsim 100$ μK.

After optimization of the mode matching of laser cooling stages and optical trapping, we end up with around 2×10^7 atoms at a temperature of ~ 80 μK.

Hyperfine pumping to the F=1/2 manifold is carried out by turning off the D1 repumper light 25 μs before the cooling light. The pumping slightly heats up the sample by a 10% of the temperature.

Evaporative cooling

The next step consists in an evaporative cooling process. It is done by ramping down in following steps the intensity of both IPG and Mephisto beams indipendently, and results with the main confinement of atoms done by the Mephisto light.
Multiple radio-frequency sweeps resonant with the $((1/2; -1/2) \leftrightarrow (1/2; +1/2))$ transition are needed to create the favourable incoherent balanced spin mixture that allows momentum redistribution among atoms thanks to collisions, suppressed by Pauli bloking in presence of a unique populated quantum state.

During this stage the Feshbach magnetic field is ramped on[1] in about 30ms up to 840 G, close to the resonance.

The evaporation is carried forward via consecutive decreasing ramps of the beams intensity. Times, target intensity and decreasing trend of each ramp are experimentally chosen by minimizing the resulting temperature. The average lasting time of each ramp is of hundreds of ms.

Main features of the obtained sample in the three Feshbach regimes

As already said, the first ramp is done at 840 G. Here atoms are strongly interacting, thus allowing to reach high efficiencies for the evaporative proces. The following evaporation ramps are carried on at different Feshbach fields, depending on which regime has to be investigated: BEC, unitary gas, BCS. To realize a BEC of tightly bounded molecules, the Feshbach field is ramped towards lower values, first down to 800 G, where the S-wave scattering length between the two species ($F_m = \pm 1/2$) is of the order of 11000 a_0, thus heigh enough to efficiently lead to three-body recombination processes as soon as the temperature becomes comparable with the molecular binding energy. A second sweep adiabatically brings the Feshbach magnetic field to the target value of 690 G.
Similar procedure is used to create unitary gases or BCS-gases, by sweeping the magnetic field from 840 G up to the decided target value.

The final trap configuration is within a very good approximation harmonic with the following typical values of dipole oscillation frequencies in

[1]The Feshbach field introduces an additional confining effect in the x-z plane (transversal to gravity) for the high-field seeker states [33]. For example, at 834 G this confinement corresponds to a frequency $\omega_B = 2\pi \times 8$ Hz. This residual curvature is due to the fact that the two Feshbach coils are placed at a distance smaller than the Helmoltz configuration. According to the Maxwell's equations, along the y-direction is instead produced an anti-confining magnetic curvature (anticurvature), that is added to the effect of gravity.

ω_x^0 Hz	ω_y^0 Hz	ω_z^0 Hz
150(3)	180(5)	14.0(0.2)

Table 4.4: Typical values of dipole oscillation frequencies of the cloud within the gas

the three directions:
These values are actually slightly different in the three Feshbach regimes, owing to the dependence of the cloud size on the the interaction parameter $1/(k_F a)$. A typical value for the Thomas-Fermi radius in the BEC regime is $R_{TF} \sim 140\ \mu$m, while at the crossover the cloud is larger with $R_{TF} \sim 260\ \mu$m, and the expansion increases with the magnetic field, up to the BCS limit where one finds $R_{TF} \sim 300\ \mu$m.

The final temperature of the cloud $T \lesssim 100\ \mu$K is low enought to assure a high level of degeneracy throughout the whole crossover, with $T/T_S \sim 10^{-2}$, where $T_S(\frac{1}{k_F a})$ is the superfluid transition temperature [38].
The total number of atoms per spin generally obtained in the ODT at the end of the preparation procedure is of the order of $\times 10^5$. In figure 4.2 I show an example of imaged cloud in the BEC limit at 690 G. In the figure it is evident the effect of the repulsive green-light sheet, extending in the x-y plane, parallel to the line of sight of the observer.

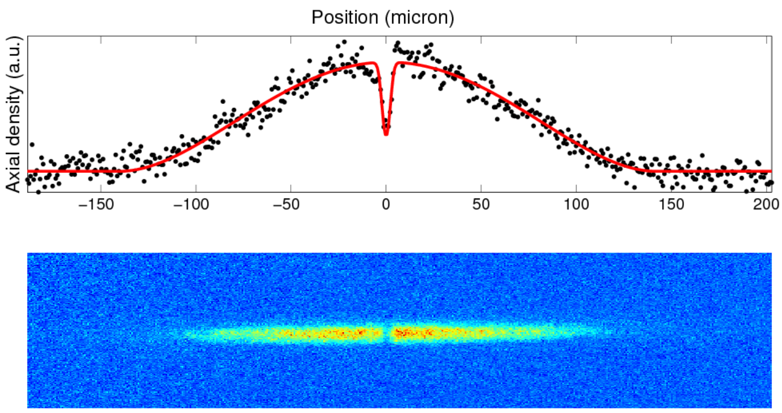

Figure 4.2: Molecular BEC imaged in situ at 690 G. The relative density profile is also shown.

4.2 Splitting of the Sample in two Reservoires: Creation of a Thin Optical Barrier Potential

The optical barrier potential is created by focalizing onto the atom cloud a sheet of light perpendicularly to the elongated direction of the sygar-shaped trap (see fig.4.2). The light has wavelength 532 nm, blue-detuned with respect to the ($2^2S \leftrightarrow 2^2P$) transition around 671 nm. The light therefore repels the atoms, splitting the cloud in two reservoires.

The height of the barrier potential V_0 felt by the atoms is tuned via analog control of the laser beam intensity.
The power of the beam is ramped up to the target value during the evaporation procedure, in order to complete the condensation of the gas in the final double-well potential trap arrangement. The raising ramp lasts 100ms, a time that is longer than the oscillation period along the trap direction $\Delta T \sim \frac{1}{14}\mathrm{s} \simeq 71$ ms, thus sufficiently slow to avoid spurious excitation of the sample.

In this section I present the experimental setup used to create and focalize the barrier onto the atom cloud. The system is sketched in figure 4.3 and 4.4.
The light beam is derived from a Verdi V8 laser, controlled in amplitude via an AOM and afterwards coupled into an optical fiber to send it to the focalization system.
The amplitude stabilization is assured by a Stanford PID (SIM 960), which compares the signal from a pick-up beam with the value set via the control program. The pick-up beam is reflexed by a thin glass (G) and recorded by a fast Thorlabs photodiod DET 36 A/M (biased Si detector, 350-1100 nm)[2]. The PD has resulted to perfecly stabilize the amplitude up to 10 kHz rumor signals; afterwards, some distorsions are observed. This upper threshold is adequate to our system, namely it is very high with respect to the typical oscillations frequencies of the atom cloud within the trap potential (see table in section 4.1).

In output from the fiber a $\lambda/2$ plus a polarizing beam slpitter stabilize the beam polarization. The beam is afterwards collimated by the two lenses L^1_{barr} (AC-508-100A, achromat 2" lens) and L^2_{barr} (LA-1384-A), with focal respectively of 100 mm and 125 mm.

[2]PD DET 36 A/M has got a rise time of 14 ns and an active area of 3.6x3.6 mm^2. It is a battery charged PD. I refer to ref. [59] for further specifications.

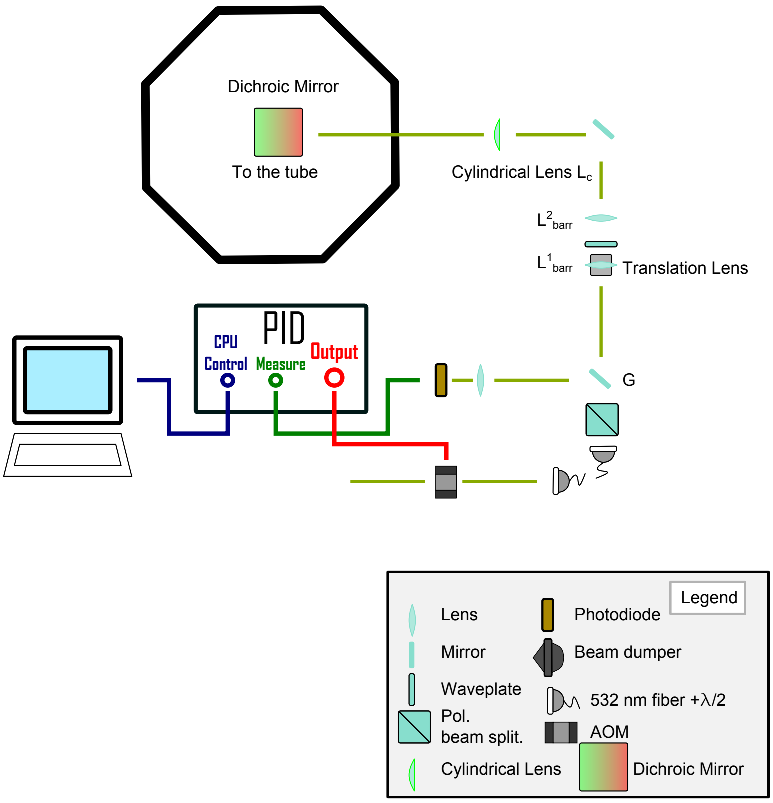

Figure 4.3: Top view of the system used to create the potential barrier and stabilize it.

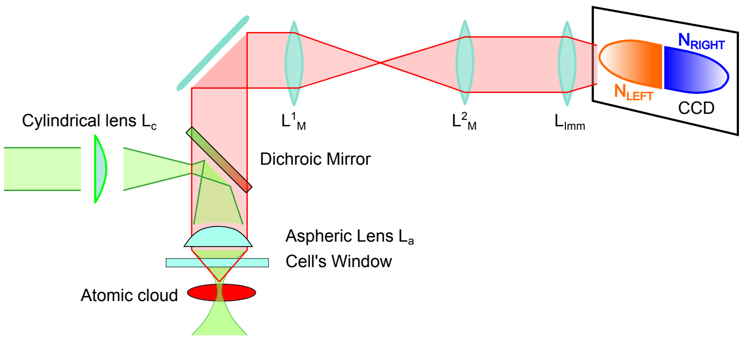

Figure 4.4: Sketch of the high resolution optical system used to imprint the barrier onto the atom cluod and to image it. The dichroic mirror allows to overlap the barrier light with the imaging one.

After the collimator system a 2" cylindrical lens L_C (LJ-1267L1) assures a strong anisotropy in the waist of the beam in the two transversal directions, with $W_z \ll W_x$. The axis labels are consistent with their resulting projection onto the atom cloud. From now on, I will always refer to z as the direction in which the sygar-shaped atom cloud is elongated, and to x and y as the transversal directions, where y identifies the gravity direction. The strong anisotropy of the transversal profile due to L_C results in a sheet-like configuration of the beam perpendicular to the z direction.
A mirror and a second 2" dichroic mirror bring the beam onto a system composed in sequens by a 2" wire grid polarizer (WGP), a 2" $\lambda/4$ and a 2" plano-convex aspheric lens AL4532 (L_A) with focal $f = 32$ mm. The aspheric lens focalizes the green light beam onto the atom cloud.

The focalization optical system for the green light is the same used to recollect the 670 nm imaging light from the cloud, as indicated by the arrows in figure. The dichroic (D) allows to separate the two beam paths by reflecting dawnwards the green light onto the aspheric lens and transmitting upwards the imaging light towards the imaging system. The numerical aperture of L_A is NA$= 0.612$ thus yelding a high theoretical resolution $R = 0.6\lambda/\text{NA} \sim \lambda$, where λ is the incident light wavelength, thus approaching the diffraction limit.

To the green light beam and imaging beam is also superimposed the upward path of the vertical MOT light in the vacuum chamber. The WGP and the $\lambda/4$ act as a retroreflecting mirror for the MOT beam while transmit both the barrier light and the imaging light. This is done thanks to the perpendicular polarization of the MOT beam with respect to the polarization of both the green light and the imaging light. The maximization of the transmittance of the green beam through the WGP is obtained by adjusting the $\lambda/2$ placed between the two collimimating lenses L^1_{barr} and L^2_{barr}. A compact cilindrical holder keeps the system composed by WGP, $\lambda/4$ and aspheric lens in the correct position and is integrated within the vacuum cell. The focalization and imaging light collecting system is shown in detail in figure 4.5. A transversal image of the green light beam in out of L_C taken with a CCD camera is also reported.

The focalization of the green light onto the atom cloud is optimized by adjusting the position of the lens L^1_{barr}, which is collocated on a traslator stage. Moreover, the cylindrical lens L_C is mounted on a rotating frame that allows to eventully change the orientation of the sheet of light with respect to the atom cloud in the x-y plane.

Finally, the high resolution imaging system is composed by a $f = 250$ mm lens L_{imm}, a two lens magnification system $(L^1_M + L^2_M)$ (of focal 150 mm and 250 mm respectively) and a EMCCD iXon3 Andor camera. The

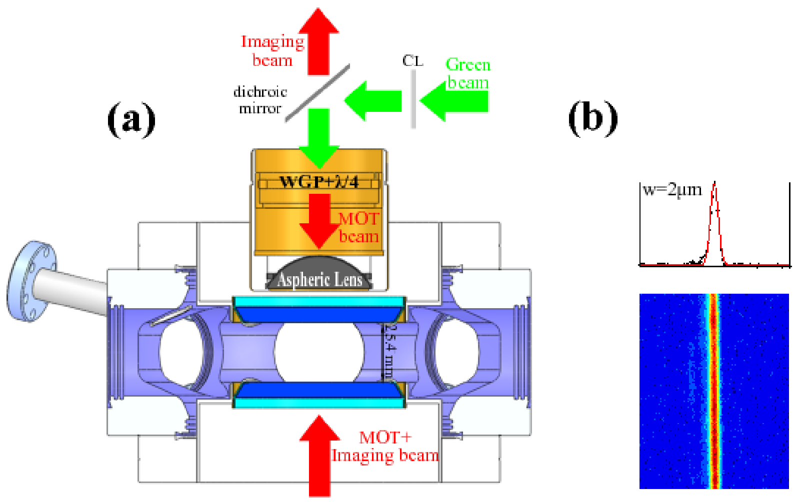

Figure 4.5: (a) Focalization and imaging light collecting system. The superimosed paths of green light, imaging light and MOT beam are indicated with arrows. (b) transversal image of the green light beam in out of L_C taken with a CCD camera is also reported.

magnification of the whole imaging system is $M = 12$.

4.3 Characterization of the Thin Optical Barrier

A first test of the actual shape of the resulting sheet-like laser beam has been done in the Master thesis [56]. I present here a detailed characterization of the beam carried out outside from the vacuum cell. I also report the experimental procedure I used to focus the barrier *in situ* onto the atom coud within the vacuum cell.

4.3.1 Characterization of the optical barrier out of the vacuum cell

To directly characterize the barrier beam I deviated the light path right afterwards the cylindrical lens L_C and reproduced on the breadboard a specular configuration to that used to focalize the barrier onto the cloud, namely I have measured the distance between the cylindrical lens L_C and the aspheric lens L_A collocated in the rigid cylindric holder of figure 4.5[3], and then placing on the breadboard a second aspheric lens identical to L_A at the same distance from the cylindric lens. The distance is ~47 cm. In the focus of the aspheric lens a CCD images the beam profiles.

Determination of W_z in the focus

First af all I determined the waist W_z placing the CCD in the z-direction focus of the aspheric lens, that means in the same position as that of the atom cloud.
To do so, I monitored the variation of the quantity as a function of the CCD position within a range of $\sim$ 600 μm around the focus. A micrometric translator has allowed sampling intervalls of $\sim$ 20 μm. The experimental results are plotted in figure 4.6. In the inset are also reported the respective mesured values for W_x. The beams results on the CCD to be Gaussian in

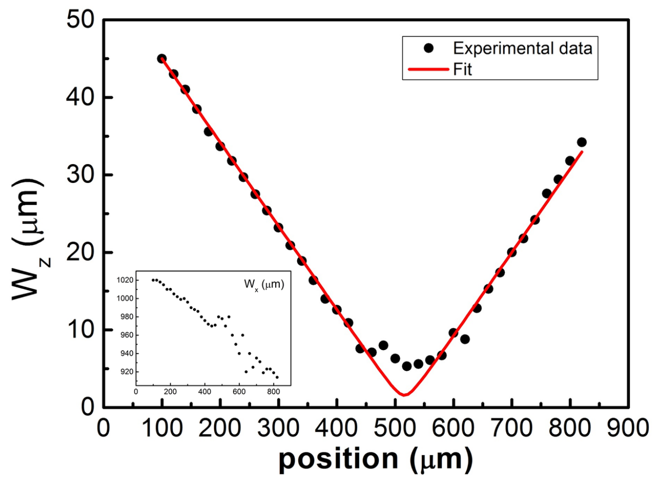

Figure 4.6: Variation of the thin waist W_z as a function of the CCD position around the focus of the aspheric lens. In the inset is also reported the variation of W_x.

both direction, thus one can fit the data with the following function

$$W_z(y - y_{off}) = W_z^0 \sqrt{1 + \left(\frac{y - y_{off}}{y_R}\right)^2} \tag{4.1}$$

[3]The holder is partially inserted into the vacuum cell. However its dimensions are known as well as the position of the aspheric lens in it. Thus it has been possible to calculate the overall path of the laser beam.

where $y_R = \pi W_0^2/\lambda$ is the Rayleigh range, with $\lambda = 532$ nm the wavelength and W_z^0 the value of the waist in the focus.
The fit yelds a value of 1.56(1) μm for the z direction. From the graph in inset one can also derive that the value of the x-direction waist changes around a value of ~ 840 μm of approximately 12% in the region of interest around the focus in the z-direction. The atom cloud dimension in the transversal directions are of the order of ~ 10 μm, namely up to two order of magnitude less than the W_x waist. Thus such a variation is actually not influencing the geometry of the system. The disagreement of the fit with the experimental data at the minimum of the trend is due to the maximum resolution of the CCD camera, namely the pixel dimension, thus larger than the expected beam waist.

Determination of W_x

I repeated the above procedure for the detemination of W_z at different distances of the aspheric lens from the cylindrical lens. For each value of W_z I have also recorded the W_x value in the minimum position for W_z. The obtained results are plotted in graphs 5 and 4.8.
I have fitted both the curves with the hyperbolic function:

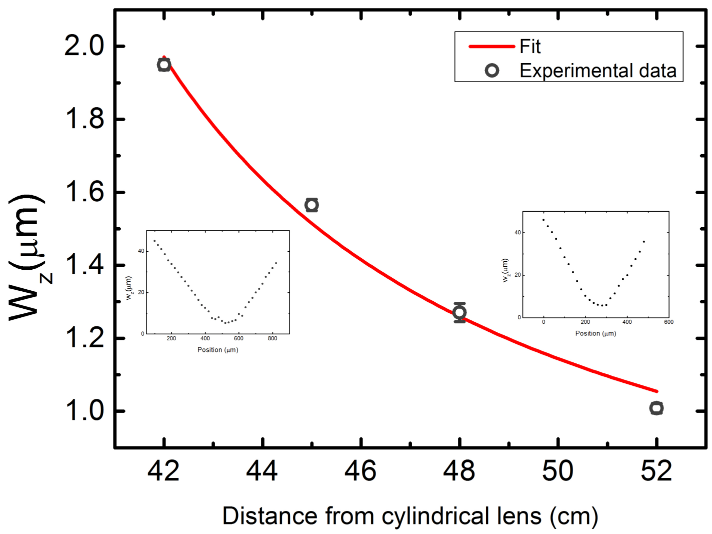

Figure 4.7: Minimum waist W_z as a function of the aspheric lens distance from L_C lens. Errors are yeld from fit.

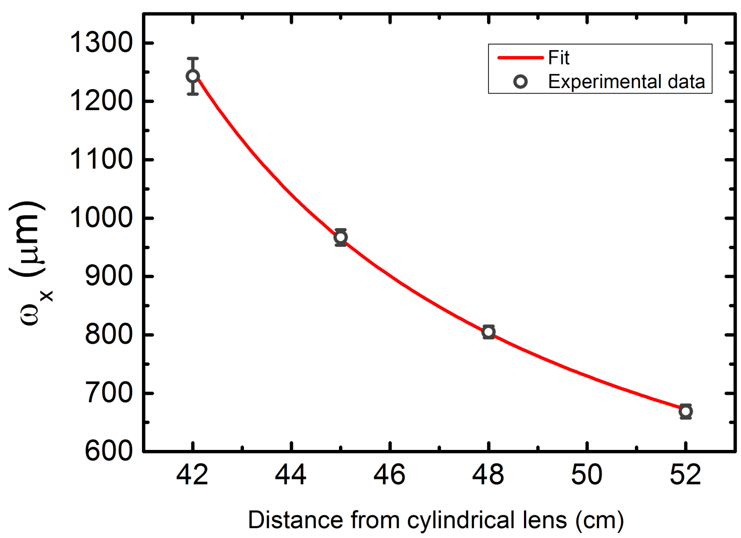

Figure 4.8: W_x as a function of the aspheric lens distance from L_C lens.

$$W(d) = \frac{Ad}{B+d} \tag{4.2}$$

where A and B are fitting parameters and d identify the distance between the two lenses.

From the parameters obtained for W_x and assuming a distance between the aspheric and cylindrical lenses to be 47.0(5) cm, one obtains an estimate of the x-direction waist in the atom cloud position of $W_x = 846(27)$ μm.
A check for W_z via the same procedure can also be done, yelding $W_x = 1.34(8)$ μm. The result is in qualitative good agreement with the direct mesurement of the waist explained in the previous section, thus confirming the adequate accuracy for the detection of the waist in the x-direction.

4.3.2 Characterization of the Barrier within the Vacuum Chamber

The characterization procedure reported in the previous section cannot account for possible distorsions introduced by the entrance window of the vacuum cell. To overcome this issue, I also extrapolated the beam size by imaging the in-situ density profile of a molecule BEC in the presence of the barrier potential. According with the local density approximation, the density depletion of the Bose Einstein condensate is directly connected with the barrier profile. However, the diffusion of atoms during the imaging pulse over micrometer scale is expected to distort and eventually broaden the barrier profile carved within the superfluid density. To overcome this issue, we acquired in situ images of the barrier imprinted on the cloud for different imaging pulse durations, and we extracted via a Gaussian fit of the depleted region the size of the barrier potential. The results are presented in Fig. 4.9. By extrapolating the beam waist of the green sheet of light down to zero pulse duration, we could infer the real size of the repulsive beam inside the vacuum cell, that results to be $W_x = 2.0(2)$ μm. Hence, the effect associated with the propagation of the beam through the re-entrant window is found to be on the order of 30%.

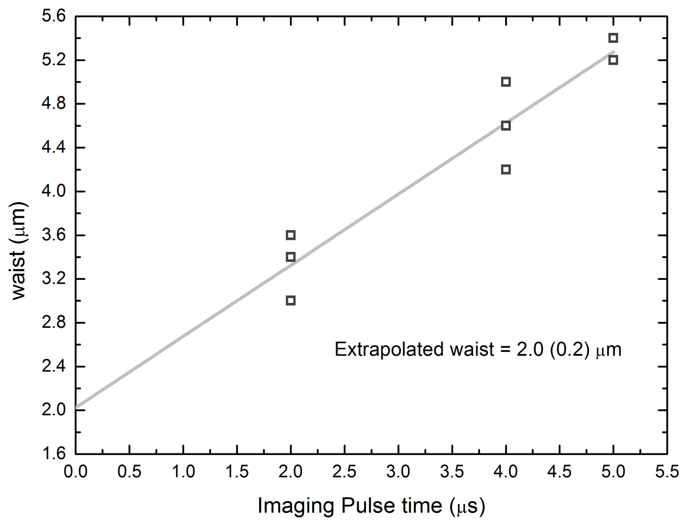

Figure 4.9: W_x deteremined from a Gaussian fit of the density depletion of a molecular BEC, as a function of the imaging pulse duration. The extrapolation of the waist to zero pulse time, gives a value $W_x = 2.0(2)$ μm.

4.3.3 Focusing of the optical barrier *in situ*

To finely tune the optical focusing system of the barrier onto the atoms I studied the transmission mechanism of atoms throughout the two reservoires. With the same procedure explained in more details in section 4.4.1, I accumulated a sourplus of atoms in one reservoir with respect to the other by

raising the barrier in a displaced position with respect to the ODT center while the gas is cooling down, and afterwards shifting the ODT center to coincide with the barrier position (see fig. 4.11). After the displacement, the system is let evolve for a time $\Delta t = T_0/2$, where T_0 is the period of the dipole oscillation (in absence of barrier) within the trap in the z-direction. After that time system is imaged and one can record the number of atoms remained in the overloaded reservoir.
I repeated the procedure adjusting the L^1_{barr} collimating lens in a ~ 2 mm space interval and recording for each position the remained atom number. The experimental reslut, obtained for a gas of molecules in the BEC regime, is reported in graph 4.10 for two values of barrier power (4.75 mW and 10 mW). I assumed that the minimum transfer of atoms from the overloaded

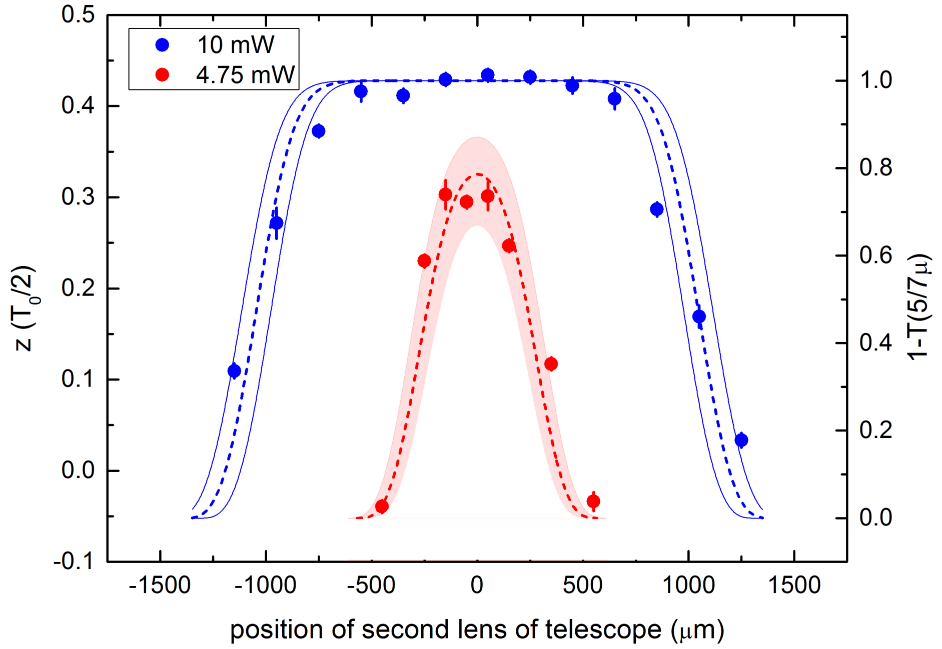

Figure 4.10:

well to the other one correspond to the maximization of the focusing of the barrier. That means in graph 4.10 the maximum of the curve corresponds to the optimal lens position.
To test the validity of this assumption I theoretically tested the variation of tunneling probability as a function of the barrier waist W_z within a very simple model. The main assumptions of the model are listed in the following:

- 1D
- non interacting bosons (single particle approximation);
- homogeneous gas;
- tunneling across a square barrier of size b and height V_0.

The size b is related to the collimation lens position p through the real barrier waist $W_z(p) = W_z^0\sqrt{1+\left(\frac{p/13}{z_R}\right)}$, where W_z^0 is the minimum waist, z_R the Rayleigh range, and p the lens position. The factor 1/13 is introduced to take into account the fact that that a displacement of Δp of the collimating lens corresponds to a $\Delta p/13$ displacement of the focalizing aspheric lens.
Given an initial energy ϵ of the particle freely moving on a side of the barrier, I have assumed that the effective size of the square barrier felt by the particle is the size of the gaussian barrier relative to ϵ, namely $b = W_z(p)\sqrt{2}\sqrt{\ln(V_0/\epsilon)}$ where V_0 is the barrier potential.
Also the maximum barrier height felt by the atoms depends on the focusing of the waist through the relation:

$$V_0 = C\frac{0.51P_0}{W_z(p)W_x} \tag{4.3}$$

where P_0 is the power of the green laser beam set by analogic command, and the constant C depends on the interaction properties of ^6Li with the radiation. The factor 0.51 accounts for the power fraction absorbed by the optics included in the beam path and for the conversion factor between the set power via analog command and the real power measured in out of the laser. In the model the waist on the x-directin W_x is assumed constant.

With these assumptions, the transmission probability $T \equiv \frac{|\Psi_1(b/2)|^2}{|\Psi_2(-b/2)|^2}$ is:

$$T(P_0,p,\epsilon) = \frac{1}{1+\frac{W_z}{2\sqrt{2}}\left(\sqrt{\frac{\epsilon}{V_0}}+\sqrt{\frac{V_0-\epsilon}{\epsilon}}\right)^2\sinh^2\left(\sqrt{\frac{2M}{\hbar^2}(V_0-\epsilon)}\right)\sqrt{\ln(\frac{V_0}{\epsilon})}} \tag{4.4}$$

Within this model, the number of atoms that remain in the overloaded reservoir is proportional to the quantity $R = [1-T]$. In order to test the goodness of the focusing method I presented above, I plot in figure 4.10 $R(P_0,p)$ as a function of the position of the collimating lens p, equating the energy ϵ to that of the energy per particle in a weakly interacting bose gas, namely $\epsilon = \frac{5}{7}\mu_B$ (see eq.(3.6)). The minimum waist has been set $W_z^0 = 2\ \mu$m.

The central lines correspond to the nominal power P_0, to which an uncertanty of 5% has been associated.

Despite its simplicity, one observes that the model is in qualitative agreement witht he experimental results. The minimum transmission of atoms is found for $p = 0$, that, having $W_z(p) = W_z^0\sqrt{1 + \left(\frac{p/13}{z_R}\right)}$, corresponds to the maximum focusing of the barrier onto the cloud.

4.4 Experiments with a Double Well: Diagnostics

4.4.1 Barrier Displacement and Dynamics Initialization

To initialize a dynamics we first set a non-zero initial imbalance $z_0 = \frac{N_1 - N_2}{N}$ (with N_1 and N_2 the atom numbers in the two reservoires) ramping the barrier at a shifted position with respect to the ODT center. The displacement between the barrier position and the ODT center is obtained by adjusting the ODT position -and not the barrier- by means of an analog control on the AOM frequency in out of the IGP laser beam.

It is very important to note that whatever displacement has been chosen, the total system of the two splitted reservoires is found in a state of equilibrium, with the internal energy characterizing the left reservoire equal to that of the right reservoire. In order to set off the dynamics, as it has been described in chapter 3, an energy difference has to be set. This is done by re-aligning the ODT center to the barrier position via the frequency AOM analog control, as sketched in figure 4.11.

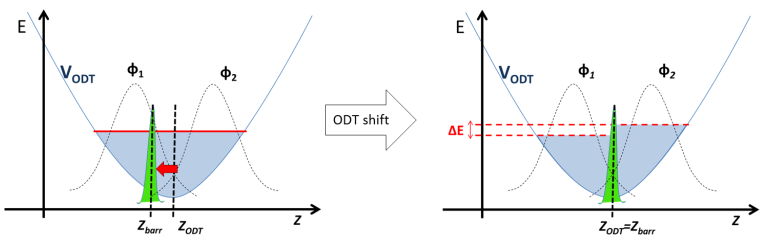

Figure 4.11: The imbalanced arrangement of the two superfluids within the double-well potential is obtained by shifting in the z-direction the ODT center position back to the symmetric configuration. Due to the different atom number between the left and right reservoires, an energy difference is set.

The shift to the final symmetric configuration with imbalanced atom number can be done both non-adiabatically, by istantaneously displacing the ODT towards the barrier position, or adiabatically, by displacing the trap in a time that is long (150 ms) with respect to the dipole oscillation period (~72 ms) of the cloud in the trap. In the second case we first rise the barrier at a high value to suppress the tunneling, and after the ODT displacement we lower it down in 2-5 ms to the target value. With this second procedure, no motion of the center of mass is excited. The relative experimental sequence is sketched in figure 4.12.
We experimentally observed the same results with the two procedures.

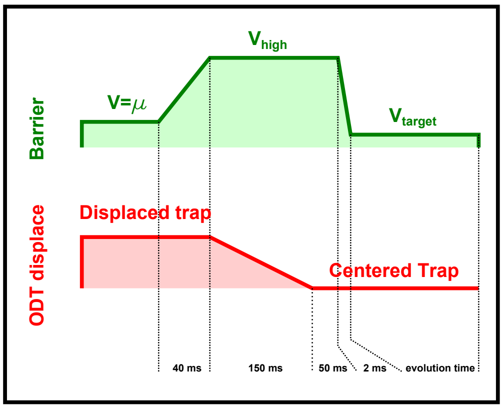

Figure 4.12: Displacement experimental procedure without excitation of dipole mode.

4.4.2 Experimental Protocols for the Dynamics Characterization

The aim of the experimental observations is that of characterizing the time evolution of the two weakly interacting superfluids system at variuos Feshbach regimes in presence of a tunable barrier, after that the dynamics is set off as descrived in the previous paragraph.
As already exlained in chapter 3, two quantities completely describe the coherent oscillations across the weak link: the population imbalance $z(t) = \frac{N_1(t)-N_2(t)}{N}$ and the relative phase $\theta(t) = \theta_1(t) - \theta_2(t)$.
In the regime in which $\Lambda > \lambda_c$, as discussed in 3, the two-mode approximation ends to correctly describe the system, and other phenomena, as the appearance of vortices, are observed.

To quantitativly describe the dynamics in all the possible situations, three main experimental observation procedures have been carried out:

- record of the evolution of $z(t)$;
- record of the evolution of $\theta(t)$ by means of observation of interference pattern in time of flight;
- observation of vortices in time of flight.

In this section I describe the three experimental procedures and the relative analysis I accomplished onto the data.

Evolution of $z(t)$

The time t_0 at which the ODT is shifted to the symmetic-geometry and the dynamics is set off, is taken as the time-reference point: $t_0 = 0$.
I reconstructed the subsequent evolution of $z(t - t_0 = t)$ progressively shifting the delay time at which the atoms cloud is imaged. In figure 4.13(a) I report an example of $z(t)$ oscillation in the Josephson regime. For each imaging time a statistics of ~ 4 data has been taken, leading to standard deviation errors as reported in graph.

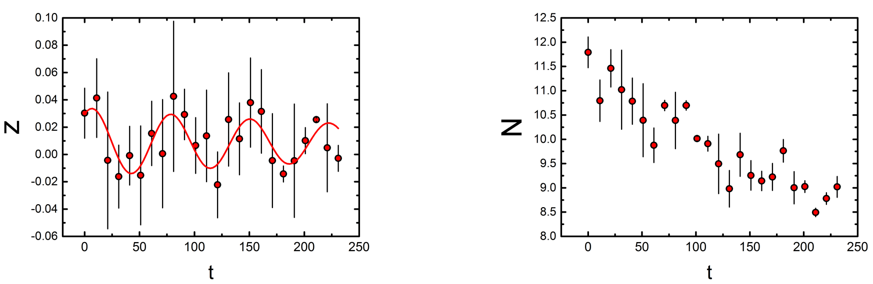

(a) (b)

Figure 4.13: (a) Time evolution of the population imbalance (x-axis units: ms). BEC regime (B=690G). Barrier power: 5mW. Initial population imbalance $z_0 \sim 0.035$. These conditions correspond to the Josephson regime. (b) Time evolution of the total atoms number (x-axis units: ms).

I also report in fig.4.13 the evolution of the total atoms number N: the investigation of the dynamics results limited to a time window of 300ms, owing to the finite life time of atoms in the trap.

Oscillations have been fitted with a sinusoidal function:

$$z(t) = off + z_0 \times e^{-\frac{t}{\tau}} \times \sin(2\pi\nu(t) + \Phi) \tag{4.5}$$

The fit takes into account a possible damping effect described by the time costant τ. This effect is the consequence of a spread in the frequency domain around the carrier frequency ν that I attribute to the finite temperature.
The phase-offset Φ has been set to $\pi/2$, having displaced the ODT so that the surplus of atoms is initially found in the left-well.
In the Josephson regime the offset in 4.5 is expected to be identically zero as it follows from relations (3.19). Nevertheless this term is also introduced as a variable in the fitting, to take into account possible systematic errors due to imaging disomogeneities, as well as the evolution to a non-zero offset value when moving towards the self-trapping regime at higher barriers.

For each set of data as in 4.13(a) the parameters in the following table have been extracted. In table are reported the numerical values related to the example of figure 4.13(a)[4].

parameter	value from fit
ν	**14.03(16)Hz**
z_0	0.019(2)
τ	–
off	0.006(2)

As a conclusion to this paragraph we point out that an analogous procedure has been used to determine the trap frequencies along the three directions, namely the oscillation frequency of the atoms cloud in absence of the barrier.

evolution of $\theta(t)$

The phase difference between the two superfluids is revealed by interference patterns as that reported in figure 4.14

The patterns are obtained in time of flight (TOF), namely both the barrier light and the ODT beams are swithced off letting the two superfluid expand and spatially overlap. The appearence of a defined interference pattern is the ultimate proof of the coherence of the two single-well states, or, in other words, that they are indeed described by an order parameter of the form (3.1) with a well defined macroscopic phase. The first experimental observation of

[4]In this example the fit does not reveal damping.

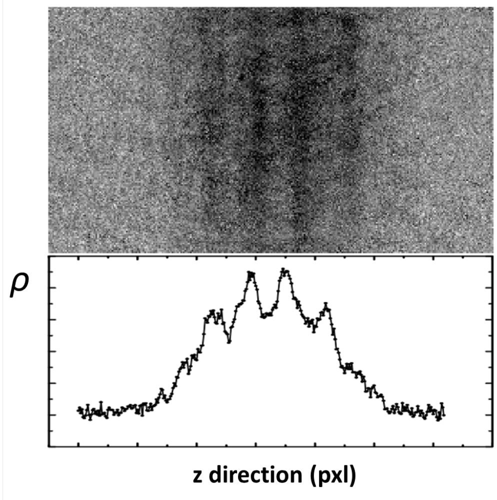

Figure 4.14: Example of imaging of the interference pattern. The corresponding density profile in arbitrary units is also shown. Unitary limit.

interference fringes was carried out by Ketterle *et al.*, 1997 for two colliding BECs [60].

The TOF expansion lasts 6 ms. In principle one would need a longer time to assure a complete overlap between the two superfluid. Unfortunatly this is not possible in our experimental configuration, because while expanding the cloud moves downwards under gravity, namely getting out from the imaging focus. I remind here in fact that the same aspheric lens is used both to focus the barrier onto the cloud and to imagine it. If one would move the lens to follow the cloud with the focus, one would also defocus the barrier *in situ*, actually decreasing the reproducibility of our experiment.

The visibility of the interference fringes in TOF has been experimentally investigated in the previous work [61]. The work prooves that the visibility of interference fringes in crossover superfluids is strongly reduced when entering the strong interaction regime, due to collision-induced dephasing. To overcome this issue and gain accuracy in the derivation of the density profile, 5-10 ms before the ODT and barrier lights are turned off the magnetic field is swept back to 690 G. The experimental sequence is reported in figure 4.15. With this procedure the interaction reduction occurs both in-trap for few ms and during the TOF. This method is similar to that used in the works [60] and [26] for the observations of vortices.

A disavantage of the procedure is that it introduces mechanical noise if the jump from the experimental Feshbach field down to 690 G is huge, hence the noise mainly affects measurements on the BCS side. The noise is sup-

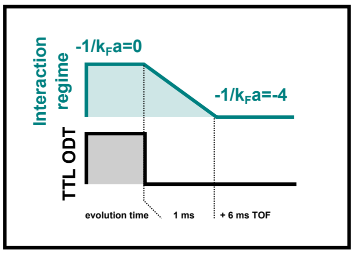

Figure 4.15: Experimental sequence used to acquire TOF phase interference patterns.

pressed by simply increasing the statistics of acquired images. Moreover the ramp to the BEC field introduces a fixed offset in the phase difference accumulated during the ramping time, but the dynamics evolution of the phase results to be not affected.

The interference patterns are fitted with a Gaussian profile modulated with a $\cos(kz + \theta)$ where θ is the phase difference. In alternative, a 1D fourier transformation of the profile has been used.

Observation of vortices in time of flight

As explained in chapter 3, in our multi-mode system the presence of the barrier may lead to the creation of vortices in the two superfluid bulks via the phenomenon of phase slippage. To investigate the occurrence of vortices, whose size is of the order of the healing length (namely $\sim 1/k_F$), I used a similar procedure used for the phase difference determination.
The main issue is to expand the cloud in TOF so that the vortices become visible while avoiding interference between the two reservoires. This is done by turning down in 30 ms the barrier height after the desired dynamics time, then holding the system in the crossed ODT for about 10 ms, to make sure that the depletion in the cloud carved by the barrier is estinguished, and finally turning off the ODT light with the gas exanding in TOF. For the same visibility issue the expansion and imaging of the cloud is done in the BEC limit. The experimental sequence is reported in figure 4.16. The presence of a vortex is determined by eye. An example of an imaged vortex is reported in figure 4.17.

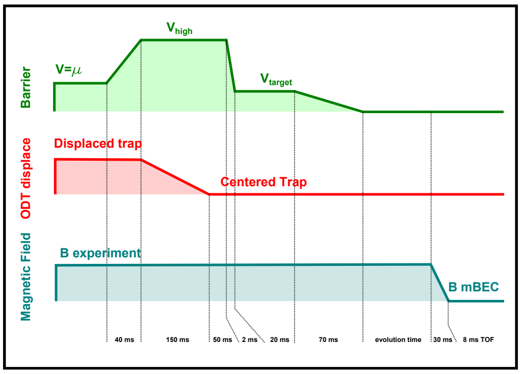

Figure 4.16: Experimental protocol for the observation of vortices in TOF.

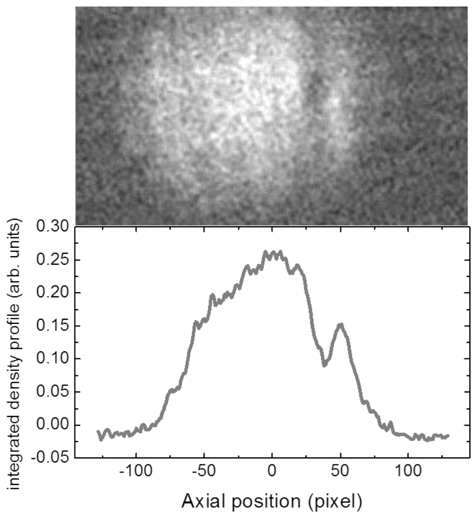

Figure 4.17: Obsevation of a vortex in the superfluid. Unitary limit.

Chapter 5

Experimental Results

In this chapter I present the experimental results I obtained by investigating the dynamics of a ^6Li crossover superfluid within a double well potential with tunable barrier height.

By controlling both the barrier height and the interaction strength between the superfluid particles, and by monitoring the system evolution exploiting the various protocols presented in the previous chapter, I could identify the boundaries between a coherent regime, where the system undergoes superfluid Josephson oscillations, and a dissipative regime, where the superfluid flow is quenched due to nucleation and propagation of topological defects within the bulk system.

5.1 Study of $z(t)$ Oscillation Frequency as a Function of the Barrier Height

A major characterization of the superfluid dynamics is based on the study of the time evolution of $z(t)$ by following the protocol described in section 4.4.2. Prior to the measurement, I determined both atom and molecule number, and the trap frequencies of the 3D harmonic potential in the absence of the thin barrier. This allows us to calculate the Fermi energy (and eventually the chemical potential) of the associated non interacting system ($E_F = (6N)^{1/3}\hbar\omega_{ho}$) and the corresponding Fermi wavevector k_F. This combined with the magnetic field dependence of $a(B)$ [24] gives the interaction strength parameter $k_F a$.

In figure 5.1 I report the time evolution of the population imbalance $z(t)$ at various barrier heights V_0 for a fixed interaction in the BEC regime ($-1/(k_F a) = 4.25(18)$). One observes that the population imbalance oscillates sinusoidally, with a frequency that progressively decreases as the barrier is set to higher values. The oscillations are clearly detectable up to a certain value of V_0. Above this critical value, no clear oscillations are observed, and $z(t)$ decreases from the initial value z_0 down to zero over a time of the order of the bare oscillation period.

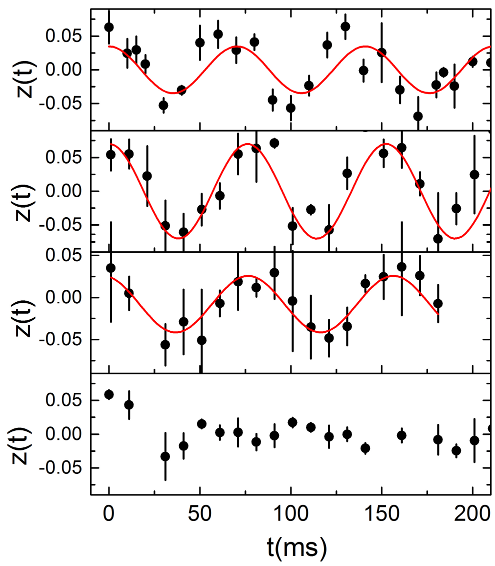

Figure 5.1: Time evolution of the population imbalance $z(t)$ at $1/(k_F a) = 4.25$, for different values of V_0/ϵ (from top to bottom: 0, 0.35, 1.15, 2.5). Initial population imbalance set at $z_0 \sim 0.04$ on a statistics of some tens of runs.

Renormalizing the extracted frequencies to the bare trap axial frequency ω_0, one can plot the ratio ω/ω_0, as a function of the barrier height V_0. In this regime, one can conveniently renormalize V_0 to $\epsilon = \frac{5}{7}\mu_B$, namely the mean energy per particle for a BEC (see eq.(3.6)). The result is reported in fig.5.2.

From graph 5.2 one can determine three regimes:

- for $V_0 < \epsilon$ the system can be considered in the hydrodynamic regime introduced in section 3.3.1. Here, the dipole oscillation frequency is only slightly modified by the presence of the barrier. In this regime the barrier potential V_0 is lower than ϵ, hence of the chemical potential of the system.

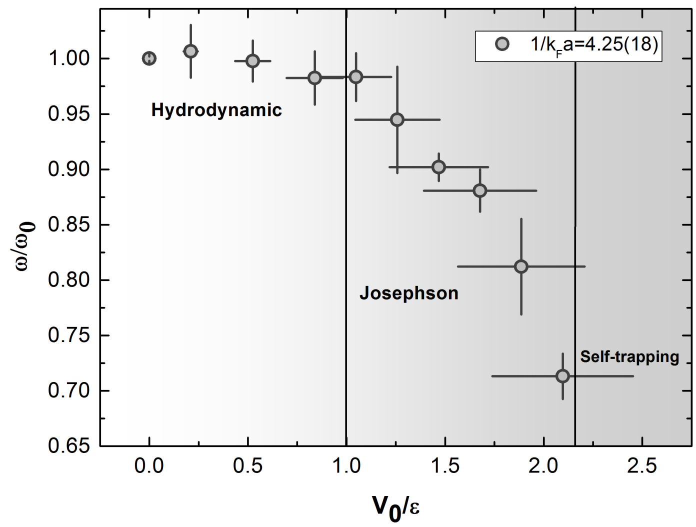

Figure 5.2: Trend of the renormalized oscillation frequency ω/ω_0 along the x-direction of the population imbalance as a function of the barrier potential height V_0 renormalized to the energy per particle in a BEC.

- For $\epsilon < V_0 < V_c$ a more pronounced bending of the oscillation frequency is observed. The system has entered the tunneling regime, in which the flow of a classical fluid would be impeded. In this case we expect that the superfluid dynamics is describable by the Josephson equations (3.22) in the limit of small oscillation amplitudes, being the intial imbalance z_0 always set well below 1, namely $z_0 \lesssim 0.06$. The two-mode model states that the frequency is given by the plasma frequency, that for sake of clarity I report here [9]:

$$\omega_p = \frac{1}{\hbar}\sqrt{2UNK + 4K^2} \tag{5.1}$$

  As theoretically predicted by eq.(5.1), the plasma frequency diminishes with increasing barrier height, since the coupling term K decreases exponentially with V_0/ϵ.

- For $V_0 > V_c$: clear sinusoidal oscillations are no longer observable. Within the two-mode model this regime corresponds to the condition $\Lambda > \Lambda_C$ (self-trapping regime), where $\langle z(t)\rangle \sim z_0$ at all evolution times. In our system however this regime is not characterized by a self-locked imbalance, as shown in the last panel of figure 5.1. In this regime the two-mode approximation does not capture, even at the qualitative level, the observed trend, which in turn suggests that the system reduces its interaction energy via some dissipation processes, as I will show in the following.

It is important to compare the trend discussed above and presented in figure 5.1 with the dynamics of an ideal Fermi gas. This has been prepared following procedures described in [57], at the zero-crossing of the 832 G Feshbach resonance, at which the interaction between $|1\rangle$ and $|2\rangle$ atoms is zeroed. In sharp contrast with the superfluid system, the normal Fermi gas presents the following trend: by progressively increasing V_0, the $z(t)$ is characterized by an increasing damping of the oscillation, while the frequency is always fixed to the bare trap value ω_0. Importantly, as soon as $V_0 > \epsilon$, in this case no coherent oscillations are observed. This behaviour can be ascribed to the presence of many single particle states of the double well potential. As soon as no particles occupy states above V_0, each fermion will evolve incoherently, leading to an overall damped $z(t)$ dynamics.

How the change of the interaction strength characterizing the superfluid affects the ω/ω_0 versus V_0 is shown in 5.3. Roughly, the data sets have been acquired with a constant atom number, trap frequencies and initial imbalance.
From these data, one can see that for each regime of the interaction, also encompassing the strongly interacting region, and up to the BCS side of the crossover, the trend is qualitatively similar to the one observed for the BEC limit, already presented in 5.2: After a slight decrease of ω/ω_0, a more pronounced bending of the curves is observed for increasing barrier heights. As for the weakly interacting BEC data, all curves cease at some critical V_0, for which the system enters in the regime of overdamped dynamics of $z(t)$.

Furthermore, one can notice that as one moves from the BEC limit towards resonance, the curves initially shift towards higher values of $V_0/\hbar\omega_0$. Qualitatively this trend can be understood if one considers that the superfluid becomes progressively more strongly interacting, hence more energetic, as the unitary limit of interactions is approached [25]. In fact, when renormalizing V_0 to the mean energy per particle at each interaction strength, all curves recorded on the BEC side of the Feshbach resonance would roughly collapse one on the other.

Interestingly, however, as the unitary point is crossed and one moves to the BCS side of the crossover, this trend ceases to hold, compare e.g. the curves relative to $1/k_F a = 0$ and $1/k_F a = -0.5$, respectively. Simply based on energetic arguments, this behavior of the curves on the fermionic side of the resonance is somewhat unexpected, since the energy of the superfluid system keeps increasing monotonically also from the unitary regime up to the BCS limit [25].

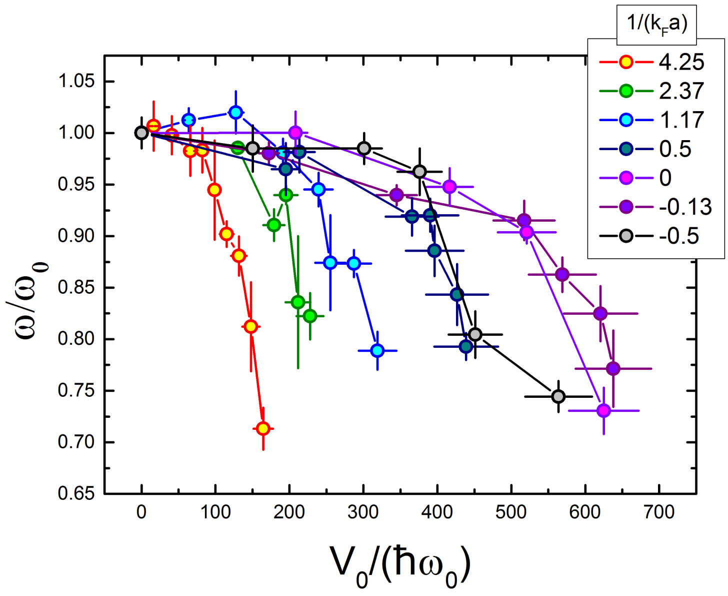

Figure 5.3: Trend of the renormalized oscillation frequency ω/ω_0 as a function of the barrier potential heigh V_0, renormalized to the energy $\hbar\omega_0$. This choice for the x-axis accounts for the effect of the variation of the dipole oscillation frequency with the Feshbach field.

5.2 Effect of the Pair Breaking on The BCS Side

In order to get a better insight into the trend occurring on the BCS side of the resonance discussed above, and also in order to get rid of spurious effects related to atom and frequency variation from one data set to the other, it is useful to re-analyze the data shown in fig.5.3 as presented in fig.5.4 Here, the experimental data are shown in a contour plot within the $1/k_F a$-ω/ω_0 plane: the different colors refer to different V_0/E_F values.

As anticipated in the previous discussion, a clear bending near the crossover region is apparent from fig.5.4 Interestingly, this behavior closely resembles the theoretical predictions for the maximum Josephson current I_0 of Refs. [19, 27, 21]. Such downward bending is ascribed in this case to pair breaking

effects, associated with the fermionic nature of the bosons composing the superfluid, and explicitely accounted in the theory.
At present, a direct comparison between our data and these theoretical prediction for I_0 is not possible, due to the lack of knowledge of the on-site interaction energy U entering the expression for the plasma frequency, given by:

$$\omega \simeq \frac{1}{\hbar}\sqrt{2UNK} \tag{5.2}$$

as reported in [27]

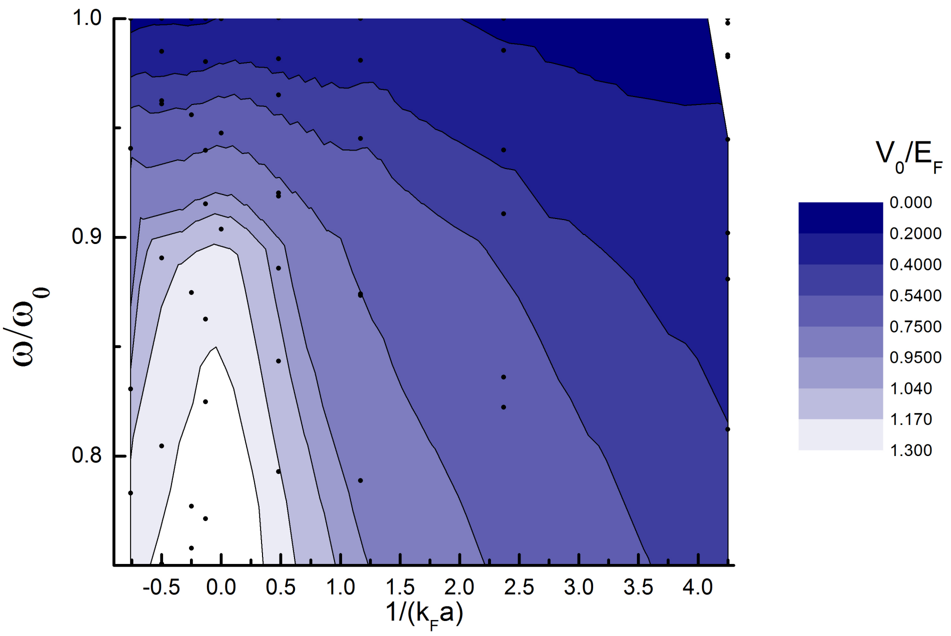

Figure 5.4: Data for ω/ω_0 plotted in the plane $(1/(k_F a); \omega/\omega_0)$: at fixed values of V_0 the oscillation frequency shows a trend inversion right on top of the crossover $(1/k_F a = 0)$. V_0 is renormalized to the Fermi energy E_F to ease the comparison with graph 3.3.

Here, K is the coupling energy term, which in turn is related to the maximum Josephson current $I_0 = NK/\hbar$ supported by the system, for a given value V_0. Nevertheless, based on the available Quantum Montecarlo and mean field theory data for the mean energy per particle [25, 17], we expect U to monotonically increase when passing from the BEC to the BCS side of the crossover. Hence, the bending down of ω detected in the experiment signals a decrease of I_0, as the fermionic excitations of the BCS superfluid start affecting the collective mode branch [44]. It is important to stress the fact that our experiment detects the fermionic nature of the bosonic pairs via the study of coherent Josephson oscillations, i.e. *without* destroying the superfluid state.

5.3 Study of $\theta(t)$ Oscillation Frequency in the Running-Phase Regime

As discussed in chapter 3, the various dynamical regimes of a superfluid evolving within a double well potential arise from the profound relation between number imbalance $z(t)$ and phase $\theta(t)$. By employing the protocol described in 4.4.2, we have also investigated the time evolution of $\theta(t)$, in the regime of coherent oscillations and in the one where overdamped dynamics of $z(t)$ is observed.
In the Josephson regime the frequency shows sinusoidal oscillations with an offset of $\pi/2$ with respect to $z(t)$, as predicted by the Josephson equations (3.22) in the limit of small amplitude. An example on the BEC side is reported in graph 5.5, confronted with the $z(t)$: one observes that the fits yeld consistet values for the two fequencies.
When entering the overdamped regime, the leakage of $z(t)$ can be in princi-

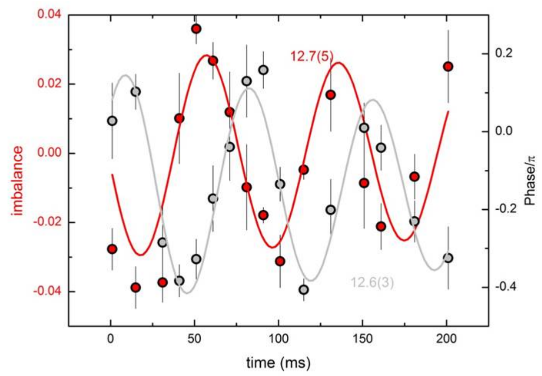

Figure 5.5: Time evolution of the phase difference $\theta(t)$ and $z(t)$ at $1/(k_F a) = 4.25$. $V_0 \leftrightarrow 4$ mW (Josephson regime). Dots: experimental data; solid lines: fit results. The two frequecy values yeld by the fit are consistent.

ple ascribed to some incoherent relaxation of the superfluid, associated with the onset of dissipation mechanisms. In order to get further information into this dynamical phase, we performed also the study of the phase evolution.

In the two mode approximation, and for $\Lambda > \Lambda_C$, the phase is expected to evolve according with the law

$$\dot{\theta} \simeq \frac{2K}{\hbar}\Lambda z \tag{5.3}$$

Namely, the phase increases linearly in time, i.e. modulus 2π, it exhibits a sawtooth evolution, with periodicity set by the difference in the chemical potential between the two wells.
Within the dynamical overdamped regime, the phase is found to evolve precisely following this trend. In figure 5.6 examples of data of the time evolution of the phase at the unitarity point $1/k_F a = 0$ are shown for three different values of the barrier height V_0. One can see that the higher the V_0, the faster the frequency of the sawtooth. In particular, in correspondence of the highest barrier height, the frequency of the oscillation is found to perfectly match the estimated chemical potential difference $\delta\mu$ initially set between the two reservoires. I remember that the phase patterns are imaged at 690 G, on the BEC limit. It is worth noting that at the crossover the observed phase at high barrieres runs with a frequency that is in agreement with the $\delta\mu$ at resonance. This means that the ramp of the Feshbach field to the BEC side to increase the visibility of the interference fringes (see section 4.4.2) does not affect the frequency at which the phase evolves.

5.4 Observation of Vortices in the Running-Phase Regime

As anticipated in section 3.3.3, a running-phase regime may be accompained by dissipation mechanisms. This is a feature of multimode systems, where the topological defect curved by the barrier potential via phase slippage mechanism has non-zero probability to detach from the barrier and propagate into the bulk.

This phenomenon is expected to appear in our system, where the typical chemical potential energy scales exceed by about an order of magnitude the transverse dipole oscillation energies $\hbar\omega^0_{x;y}$. This implies that even for the small imbalances z_0, the double well (axial) dynamics can induce excitations along the transverse directions. In order to check whether and how such topological defects enter in the superfluid bulk, we performed a detailed study of the system dynamics by exploiting the protocol of section 4.4.2.
From this investigation, we interestingly found out a one-to-one correspondence between the occurrence of topological defects in the bulk and the en-

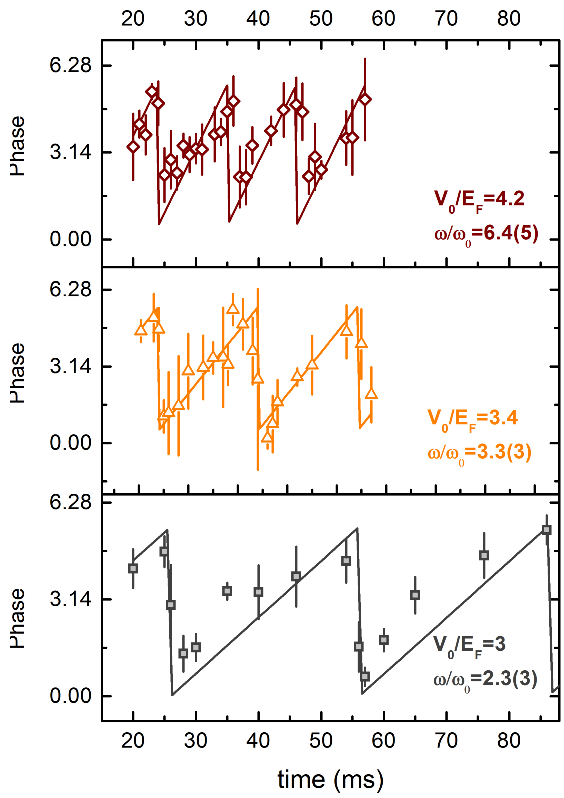

Figure 5.6: Time evolution of the phase difference $\theta(t)$ at different values of the barrier heigh V_0 at the unitary limit. V_0 is renormalized to the Fermi energy E_F. Dots: experimental data; solid lines: fit results.

trance in the running phase, overdamped regime signalled by the absence of $z(t)$ oscillations. This close connection is presented in 5.7: here, the occurrence of topological defects is contrasted with the behavior of ω/ω_0 as a function of the increasing barrier height. From this comparison, it is clear that a non-zero occurrence of defects in the superfluid bulk is present only when the overdamped, running phase is reached.

In principle, the nature of such defects could be various. In order to better identify them, we have characterized their oscillation frequency within the cloud. To do so, we initially created the defect by setting the barrier at a height where we previously observed a high occurrence of the defect in the bulk. We then switched off the barrier, and varied the time in which the system is held in the ODT without barrier, while the defect propagates in

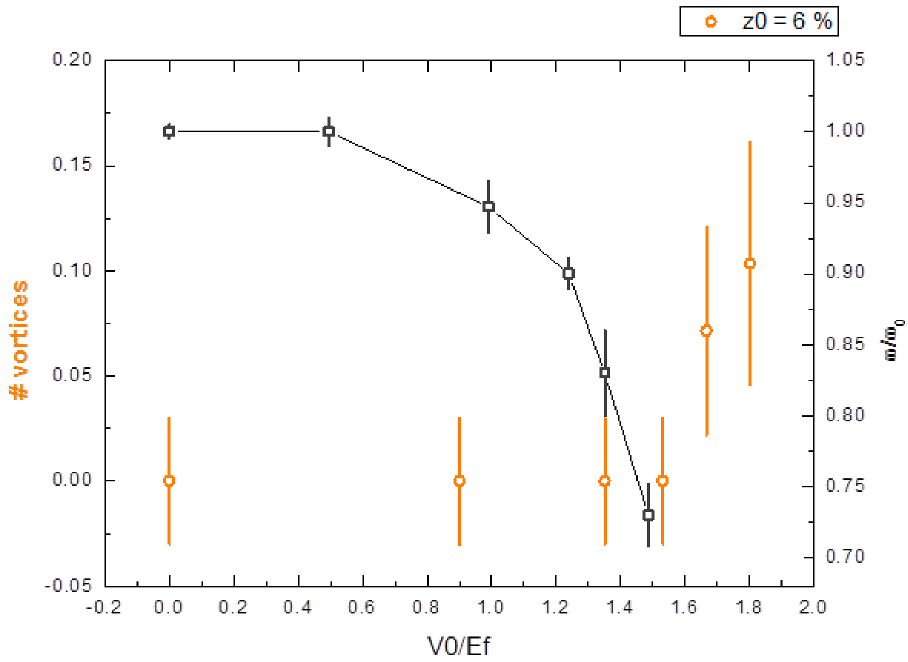

Figure 5.7: Confront of the occurrence of vorties with the oscillation frequecy of $z(t)$ as functions of the barrier heigh at $1/(k_F a) = 0$. Again V_0 is renormalized to the Fermi energy. Data taken for an average initial imbalance $z_0 \sim 0.06$ (standard deviation errors reported). The average number of vortices is obtained over a statistics of 20-30 images (standard deviation errors reported).

the superfluid. After this variable time, the ODT was switched off, the cloud was expanded in TOF and finally imaged.
By recording the position of the defect with respect to the center of mass position of the expanded cloud, we obtained an oscillatory motion along the axial direction of the trap. We repeated this measurement at different interaction strengths, and the results are shown in fig.5.8.

Our data show a strong dependence of the oscillation frequency of the defect on the value of the interaction strength, and it is found in excellent agreement with the experimental results in Ref. [26, 29], that identified those defects as being solitonic vortices.

In order to get further insights in the occurrence of solitonic vortices within the superfluid as a function of the system parameters, I present in fig.5.9 experimental data that show how the onset of defects in the bulk de-

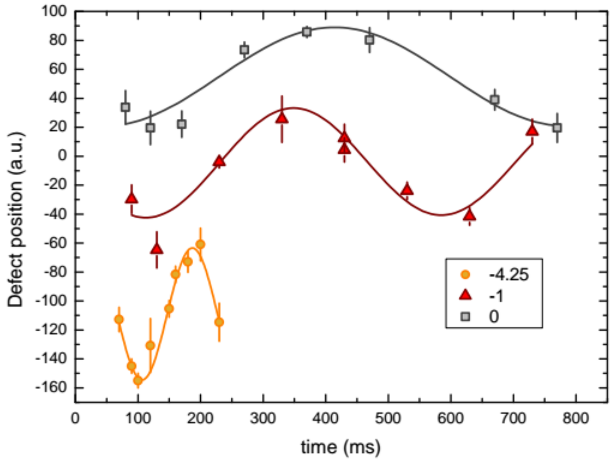

Figure 5.8: Time trajectories in the z-direction of the topological defect observed at $-1/(k_F a)$=-4.25; -1 and 0, as indicated in the inset.

pends on (a) the initial imbalance and (b) on the barrier height.
From this characterization, one can see that the data in fig.5.9 are in qualitative agreement with the expectation derived from the two-mode approximation, which predicts the onset of the running phase regime to be determined by the relation

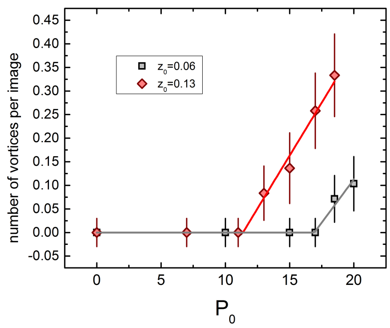

(a)

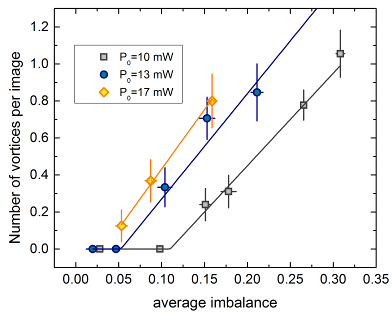

(b)

Figure 5.9: (a) Study of the occurrence of vortices in the bulk as a function of the barrier ligh power P_0, for $z_0 = 0.06, 0.13$. (b) Study of the occurrence of vortices as a function of z_0 for three values of P_0: 10, 13 and 17 mW. Data taken at $1/(k_F a) = 0$

$$\Lambda_c = 2\left(\frac{\sqrt{1-z(0)^2}\cos\theta(0)+1}{z(0)^2}\right) \tag{5.4}$$

Indeed, an increased z_0 decreases the critical V_0 for which the critical point is reached. Analogously, an increased barrier height, hence a decreased K, lowers the initial z_0 at which the system enters the running phase regime.

Finally, we repeated the procedure followed for the acquisition of the data presented in Fig. 1.8 for different interaction strengths. The result of this thorough characterization is presented in Figure 1.10 as a contour plot within the $1/k_F a$-V_0 plane. Different colors correspond to different probability foe the occurrence of vortices in one image, averages over a data set of about 20-30 images per point. In order to speed up the aquisition of the data, we set an initial imbalance $z_0 = 0.12(2)$.

Very interestingly, the overall behavior associated with the occurrence of vortices in the bulk througout the BEC-BCS crossover perfectly mirrors the trend of the oscilation frequency derived from the study of the time evolution of $z(t)$ (see fig.5.10).

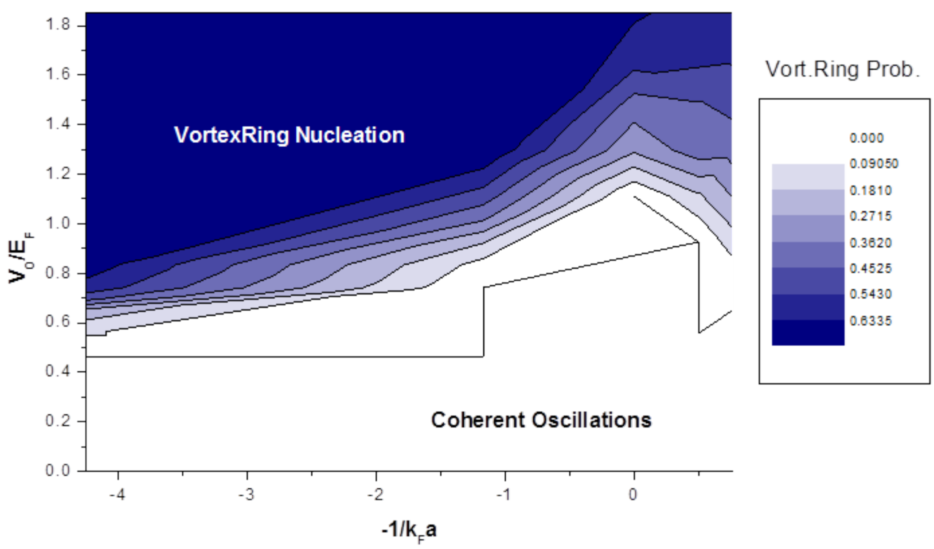

Figure 5.10: Occurrence of vortices in the superfluid bulk as a function of V_0/E_F and $1/(k_F a)$. The initial imbalance z_0 was set for this characterization to 0.12(2).

Chapter 6

Conclusions and Outlook

In my thesis, I performed the first experimental study of the dynamics of a BEC-BCS crossover Fermi superfluid evolving within a double well potential. The results obtained in this work allow us to identify two distinct dynamical regimes within the interaction strength-barrier height plane: In a first region, we observe coherent dynamics characterized by Josephson oscillations of the superfluid. Here, a one-to-one correspondence between time evolution of the number imbalance $z(t)$ and of the superfluid phase difference $\theta(t)$ across the barrier is found, in good agreement with theoretical expectations nowadays available. Very importantly, the characterization presented in this thesis provides the first experimental evidence for pair breaking effects affecting the coherent dynamics of a superfluid Fermi gas.

In the regime of high barriers, the experimental results I obtained in this work disclose a second dynamical regime of the many-body system. This second parameter region, within which no coherent dynamics of z(t) could be observed, is characterized by the superfluid phase difference linearly increasing in time. I also find that throughout the interaction-barrier plane, the running phase regime is accompanied by vortex nucleation and proliferation in the superfluid bulk. This observation is interpreted in terms of the phase slippage mechanism, together with the multimode structure of our system.

The various experimental protocols developed in this thesis allowed me to precisely characterize the boundary between those two dynamical regimes. It will be interesting in the near future to compare our experimental findings with theoretical prediction specifically developed for our peculiar superfluid system.

Future interesting studies that one can perform with the current experimental setup are various, and I briefly mention a few of them in the following.

An experimental investigation that could directly follow the work presented in Chapter 5 of my thesis is the characterization of the superfluid dynamics in the regime of large initial imbalance z0, and arbitrarily low barrier heights. This study would be especially appealing in the context of measuring the critical velocity of the superfluid throughout the BEC-BCS crossover [45, 22].

Another interesting extension of my thesis work could be the investigation of the system dynamics in the presence of a time-dependent modulation, either of the height or of the position of the barrier relative to the trap. This experiment could be regarded as the analog of the Shapiro effect in superconductor junctions [62].

Finally, another very appealing study that can be in principle performed on the experimental setup developed in this thesis, regards the investigation of the physics of the so-called upper branch of the Fermi gas (see Chapter 2). In this regime, unpaired $\uparrow$ and $\downarrow$ fermionic atoms interact with a positive scattering length: Interestingly, for sufficiently strong inter-particle repulsion, a phase transition to a ferromagnetic state is expected to occur in such a system [63, 37], leading to a macroscopic spatial separation of the $\uparrow$ and $\downarrow$ Fermi gas components in the trap. When starting with a homogeneous mixed sample, however, the investigation of such a phase transition is unfortunately hindered by strong recombination processes that rapidly depopulate the upper branch via decay onto lower-lying molecular states [64]. An alternative experimental strategy, that possibly allows to overcome such an instability issue, would be to artificially prepare the system in a ferromagnetic phase. Namely, one could initially create the $\uparrow$ and $\downarrow$ Fermi gases in two distinct potential wells, separated by a high barrier potential that impedes particle tunneling. From here, one could then study the dynamics of the system after partial or complete lowering of the barrier, as a function of the interspecies interaction. If a ferromagnetic phase would be energetically allowed, it should be unveiled by an extremely long time, during which the two components remain spatially separated, without penetrating into each other. The advantage of such an experimental configuration, is that initially at least the two components would touch only at the boundary set by the barrier, hence strongly reducing the effect of inelastic decay.

Bibliography

[1] Landau L.D. In: *J. Phys* 5.1 (1941), pp. 71–90.

[2] Feynman R.P. In: *Progress in low temperature physics* 1 (1955), pp. 17–53.

[3] Feynman R.P. In: *Physical Review* 91.6 (1953), p. 1301.

[4] Anderson P.W. In: *Reviews of Modern Physics* 38.2 (1966), p. 298.

[5] Josephson B.D. In: *Physics letters* 1.7 (1962), pp. 251–253.

[6] Abrikosov A.A. et al. In: *ZETF* 39.1781 (1960).

[7] Roditchev D. et al. In: *Nature Physics* 11.332 (2015).

[8] Varoquaux E. In: *arXiv preprint arXiv:1406.5629* (2014).

[9] Smerzi A. et al. In: *Physical Review Letters* 79.25 (1997), p. 4950.

[10] Raghavan S. Smerzi A. In: *Physical Review A* 61.6 (2000), p. 063601.

[11] Fort C. Maddaloni P. Minardi F. Trombettoni A. Smerzi A. Inguscio M. Cataliotti F.S. Burger S. In: *Science* 293.5531 (2001), pp. 843–846.

[12] Albiez M. et al. In: *Phys. Rev. Lett.* 95 (1 2005), p. 010402.

[13] Levy S. et al. In: *Nature* 449 (2008), pp. 579–583.

[14] Abbarchi M. et al. In: *Nature Physics* 9 (20013), pp. 275–279.

[15] Packard R.E. Sato Y. In: *Reports on Progress in Physics* 75.1 (2012), p. 016401.

[16] Salomon C. Inguscio M. Ketterle W. *Gas Di Fermi Ultrafreddi.* Vol. 164. IOS Press, 2007.

[17] Stringari S. Giorgini S. Pitaevskii L.P. In: *Reviews of Modern Physics* 80.4 (2008), p. 1215.

[18] Zwierlein M. Randeria M. Zwerger W. “The BCS–BEC Crossover and the Unitary Fermi Gas”. In: *The BCS-BEC Crossover and the Unitary Fermi Gas.* Springer, 2012, pp. 1–32.

[19] Spuntarelli A. and Strinati G. C. Pieri P. In: *Phys. Rev. Lett.* 99 (4 2007), p. 040401.

[20] Pu H. Adhikari S.K. Lu H. In: *Physical Review A* 80.6 (2009), p. 063607.

[21] Toigo F. Ancilotto F. Salasnich L. In: *Physical Review A* 79.3 (2009), p. 033627.

[22] Watanabe G. et al. In: *Physical Review A* 80.5 (2009), p. 053602.

[23] Chin C. et al. In: *Reviews of Modern Physics* 82.2 (2010), p. 1225.

[24] Zürn G. et al. In: *Phys. Rev. Lett.* 110 (13 2013), p. 135301.

[25] Casulleras J. Giorgini S. Astrakharchik G.E. Boronat J. In: *Phys. Rev. Lett.* 93 (20 2004), p. 200404.

[26] Yefsah T. et al. In: *Nature* 499.7459 (2013), pp. 426–430.

[27] Dalfovo F. Zou P. In: *Journal of Low Temperature Physics* 177.5-6 (2014), pp. 240–256.

[28] Abad M. et al. In: *arXiv preprint arXiv:1409.5598* (2014).

[29] Ku M.J. et al. In: *Physical review letters* 113.6 (2014), p. 065301.

[30] Lifshitz E.M. Landau L.D. *Quantum Mechanics: Non-relativistic Theory.* 1958.

[31] Köhler T. et al. In: *Rev. Mod. Phys.* 78 (4 2006), pp. 1311–1361.

[32] Radzihovsky L. Gurarie V. In: *Annals of Physics* 322.1 (2007), pp. 2–119.

[33] Joachain C.J. Bransden B.H. *Physics of atoms and molecules.* Pearson Education India, 2003.

[34] Castin Y. Pricoupenko L. In: *Phys. Rev. A* 69 (5 2004), p. 051601.

[35] Pricoupenko L. Olshanii M. In: *Physical review letters* 88.1 (2001), p. 010402.

[36] Arimondo E. Berman P.R. Lin C.C. *Advances in Atomic, Molecular, and Optical Physics.* Vol. 54. Academic Press, 2006.

[37] Bruun G. M. Massignan P. Zaccanti M. In: *Reports on Progress in Physics* 77.3 (2014), p. 034401.

[38] Zwierlein M. W. Ketterle W. In: *arXiv preprint arXiv:0801.2500* (2008).

[39] D.S. Petrov. In: *Physical review letters* 93.14 (2004), p. 143201.

[40] Kolomeitsev E.E. Bruun G.M. Jackson A.D. In: *Physical Review A* 71.5 (2005), p. 052713.

[41] Dalfovo F. et al. In: *Rev. Mod. Phys.* 71 (3 1999), pp. 463–512.

[42] Albus A. P. et al. In: *Journal of Physics B: Atomic, Molecular and Optical Physics* 35.23 (2002), p. L511.

[43] Manini N. Toigo F. Salasnich L. Ancilotto F. In: *Laser physics* 19.4 (2009), pp. 636–641.

[44] Stringari S. Combescot R. Kagan M.Yu. In: *Phys. Rev. A* 74 (4 2006), p. 042717.

[45] Miller D. et al. In: *Physical review letters* 99.7 (2007), p. 070402.

[46] Bulgac A. et al. In: *Physical review letters* 112.2 (2014), p. 025301.

[47] Pavloff N. Leboeuf P. Albert M. Paul T. In: *Physical review letters* 100.25 (2008), p. 250405.

[48] Strinati G.C. Spuntarelli A. Pieri P. In: *Recent Progress in Many-Body Theories*. Vol. 1. 2008, pp. 75–78.

[49] Raghavan S. et al. In: *Physical Review A* 59.1 (1999), p. 620.

[50] In: ().

[51] Rowell J.M. Anderson P.W. In: *Physical Review Letters* 10.6 (1963), pp. 230–232.

[52] Salgueiro A.N. et al. In: *The European Physical Journal D* 44.3 (2007), pp. 537–540.

[53] Bulgac A. In: *Science* 332.6035 (2011), pp. 1288–1291.

[54] Sukhatme K. et al. In: *Nature* 411.6835 (2001), pp. 280–283.

[55] Valtolina G. "Development of an experimental apparatus for the poduction and study of ultracold atomic gases of fermionic Lithium". In: *Master thesis* (2012).

[56] Morales A. In: *Master thesis* (2012).

[57] Burchianti A. et al. In: *Physical Review A* 90.4 (2014), p. 043408.

[58] Xhani A. "Production and observation of degenerate quantum gases of Li-6 fermionic atoms". In: *Master thesis* (2014).

[59] "DET36A(/M) Si Biased Detector User Guide". In: (). URL: `http://www.thorlabs.de/thorcat/13000/DET36A_M-Manual.pdf`.

[60] Ketterle W. et al. In: *Science* 275.5300 (1997), pp. 637–641.

[61] Kohstall C. et al. In: *NJP* 13.5300 (2011), p. 065027.

[62] Antonio Barone and Gianfranco Paterno. *Physics and applications of the Josephson effect*. Vol. 1. Wiley New York, 1982.

[63] Edmund C Stoner. In: *The London, Edinburgh, and Dublin Philosophical Magazine and Journal of Science* 15.101 (1933), pp. 1018–1034.

[64] Sanner C. et al. In: *Phys. Rev. Lett.* 108 (24 June 2012), p. 240404.